

DEVELOPMENT OF PROSTHETIC SKIN

by

ROHIT KILARU

Presented to the Faculty of the Graduate School of
The University of Texas at Arlington in Partial Fulfillment
of the Requirements
for the Degree of

MASTER OF SCIENCE IN ELECTRICAL ENGINEERING

THE UNIVERSITY OF TEXAS AT ARLINGTON

May 2011

Copyright © by Rohit Kilaru 2011

All Rights Reserved

ACKNOWLEDGEMENTS

I would like to express my sincere gratitude to my advisor Dr. Zeynep Çelik-Butler for her guidance and support throughout my research work. In my formative years as a student researcher she has given me invaluable feedback. Her excellent remarks and keen sense of observation helped me in getting the best out of my research.

I like to thank Dr. Donald P. Butler, Dr. Dereje Agonafer for taking part in my thesis committee. I am especially grateful to Dr. Donald P. Butler for his continuous help. The discussions I had with him whenever I hit a road block during the period of my research helped me immensely. I also like to thank Texas Ignition Fund grant program for their financial support.

I would like to thank the Nanofab staff: Dennis Bueno, Eduardo Maldonado, and Richard K. Chambers for their prompt attendance in troubleshooting problems with the clean room equipment.

I would like to thank my current and former group members: Dr. İsmail Erkin Gönenli, Gaviraj, Dr. Suraj Kumar Patil, Moinuddin, Iqbal, Madhumita, Clement and Bhargav for all their help. A special mention to my friends for their help in the clean room Amit Banik, Dr. Ramkumar Subramanian, Pradeep Bhadrachalam, Arvinder Singh Chadha and Liang-Chieh Ma.

I am indebted to all my family members, especially my father Dr. K. Satish Chandra, my mother Laxmi Kilaru, my brother Hemanth Kilaru and my fiancé Shweta Shankar for their love, support and encouragement.

This work is dedicated to my mother and father.

April 29, 2011

ABSTRACT

DEVELOPMENT OF PROSTHETIC SKIN

Rohit Kilaru, M. S.

The University of Texas at Arlington, 2011

Supervising Professor: Dr. Zeynep Çelik-Butler

The objective of this research was to embed tactile sensors in polyimides. This novel method could be utilized to realize a prosthetic skin for sensing different kinds of mechanical stimuli. There is a growing interest in tactile sensors in the medical sector for upper and lower-limb prosthetic applications in addition to potential industrial uses in robot end-effectors, grippers and manipulators. The sensors developed here, are targeted for prosthetic arm tactile sensing applications. Current work presents piezoresistive differential pressure sensors fabricated on flexible polyimide films or substrates.

A unique technique to bond a flexible superstrate polyimide layer to a MEMS tactile sensor array is presented in this thesis. The sensor is made of an aluminium oxide membrane layer with nichrome piezoresistors connected in a half-Wheatstone bridge configuration. Sensors with four different designs have been characterized to obtain the piezoresistive gauge factor of thin film nichrome. The sensor arrays with and without the superstrate film were simulated to obtain the maximum stress, average strain and deflection of the membrane. The maximum change in output voltage was 0.8 mV. The gauge factors calculated for tactile

sensors range between 2.2 to 7.8 for the ones with a superstrate and 1.5 to 5.7 for the ones without a superstrate.

TABLE OF CONTENTS

ACKNOWLEDGEMENTS	iii
ABSTRACT	iv
LIST OF ILLUSTRATIONS.....	viii
LIST OF TABLES	xii
LIST OF SYMBOLS	xiii
Chapter	Page
1. INTRODUCTION.....	1
1.1 Background	1
1.2 Flexible Substrate	6
1.3 Tactile Sensors.....	11
1.4 Piezoresistivity.....	15
1.5 MEMS Packaging.....	20
2. DESIGN AND SIMULATION OF TACTILE SENSORS	22
2.1 Piezoresistive Pressure Sensor: Theory of Operation	22
2.2 Wheatstone Bridge.....	23
2.3 Design of Flexible Tactile Sensors.....	26
2.4 Simulation of Flexible Tactile Sensors	27
2.5 Simulation of Flexible Tactile Sensors with Superstrate	31
2.6 Summary.....	35
3. FABRICATION	38
3.1 Fabrication of Flexible Tactile Sensors	38
3.2 Flexible Tactile Sensor Packaging with a Superstrate.....	44

3.3 Summary	47
4. CHARACTERIZATION	48
4.1 Flexible Tactile Sensor Characterization without and with a Superstrate	48
4.1.1 I-V Measurements	48
4.1.2 Response Measurements	49
4.1.2.1 Response measurements results without superstrate...	52
4.1.2.2 Response measurements results with superstrate.....	52
4.1.3 Gauge Factor Measurements	58
4.2 Discussion	59
4.3 Summary	60
5. CONCLUSION	61
APPENDIX	
A. FLEXIBLE TACTILE SENSOR DESIGNS	63
B. FLEXIBLE TACTILE SENSOR SIMULATION SETTINGS AND CALCULATIONS	67
C. FLEXIBLE TACTILE SENSOR CHARACTERIZATION RESULTS	77
REFERENCES	86
BIOGRAPHICAL INFORMATION	92

LIST OF ILLUSTRATIONS

Figure	Page
1.1 Different kinds of haptic perception	2
1.2 Tactile sensors on a flexible substrate	6
1.3 Polyimide: polymer structure. (a) Generic polyamic acid, (b) Polyimide after imidization reaction.	8
1.4 Device-film on a compliant substrate depicting the stresses, neutral plane and radius of curvature	11
1.5 Basic components of a pressure sensor	12
1.6 Hysteresis: pressure vs. sensor output	13
1.7 Representation of normal and shear stresses	17
1.8 (a) Longitudinal piezoresistance coefficient, (b) transverse piezoresistive coefficient cases	19
2.1 Solid model of the piezoresistive pressure sensor	22
2.2 Wheatstone bridge circuit diagram	23
2.3 Image of the membrane when the load is being applied using a probe-tip	24
2.4 Image of the circular undercut region in a fabricated tactile sensor	27
2.5 Clipped structure of the simulated tactile sensor	29
2.6 Load application on the 20 μm patch	29
2.7 Boundary conditions emulating the ashed sacrificial polyimide layer	30
2.8 Mises stress for a tactile sensor design T2 without superstrate	30

2.9 Mises stress for a tactile sensor design T4 without superstrate	31
2.10 Load application on the 20 μm patch of the superstrate	33
2.11 Boundary conditions of the superstrate layer	34
2.12 Boundary conditions emulating the ashed sacrificial polyimide layer	34
2.13 Mises stress for a tactile sensor design T2 with superstrate	37
2.14 Mises stress for a tactile sensor design T4 with superstrate	37
3.1 Process flow for the fabrication of a tactile sensor	39
3.2 After photolithography using LOR 15B and S1813 (a) Patterned features after photolithography, (b) Mask patterns of the trenches on the diaphragm and (c) Surface profile of the patterned features using S1813 photoresist	41
3.3 (a) Aluminium oxide membrane layer images, (b) Mask patterns of the trenches on the diaphragm and alignment mark and (c) Surface profile of the aluminium oxide membrane layer	42
3.4 Nichrome piezoresistors after lift-off.....	43
3.5 (a) After lift-off of Al metallization and (b) Magnified image of the Al metallization	43
3.6 Suspended membrane after ashing the sacrificial polyimide.....	44
3.7 (a) Adhesive polyimide being dispensed on the superstrate and (b) Tactile sensor die placed on the superstrate for heat treatment	46
3.8 Superstrate bonded to the tactile sensor die	46
3.9 Solid model of the superstrate bonded to the tactile sensor (a) 3D model of the tactile sensor with superstrate and (b) Close-up onto the edge of the bonding pads.....	47
4.1 Pseudo resistance of A_1	48
4.2 Illustration of the setup to measure the tactile sensor output	49
4.3 Change in output voltage with load vs Wheatstone bridge	

input voltage for T1 device # I without a superstrate	53
4.4 Change in output voltage with load vs Wheatstone bridge input voltage for T2 device # I without a superstrate	53
4.5 Change in output voltage with load vs Wheatstone bridge input voltage for T3 device # I without a superstrate	54
4.6 Change in output voltage with load vs Wheatstone bridge input voltage for T4 device # II without a superstrate	54
4.7 Change in output voltage with load vs Wheatstone bridge input voltage for T1 device # II with a superstrate	55
4.8 Change in output voltage with load vs Wheatstone bridge input voltage for T2 device # I with a superstrate	56
4.9 Change in output voltage with load vs Wheatstone bridge input voltage for T3 device # I with a superstrate	56
4.10 Change in output voltage with load vs Wheatstone bridge input voltage for T4 device # I with a superstrate	57
4.11 (a), (c) Mises stress simulations for device types T2 and T4 without superstrate and (b), (d) Mises stress for device types T2 and T4 with superstrate	58
A.1 Trench mask layout.....	64
A.2 Piezoresistor mask layout.....	64
A.3 Metallization mask layout.....	65
A.4 Passivation mask layout	65
A.5 Bond-pad mask layout	65
B.1 Description of U and Y shaped piezoresistors.....	69
B.2 Layout of a tactile sensor without superstrate	71
B.3 Process-file of a tactile sensor without superstrate	72
B.4 Meshed solid model of a tactile sensor without superstrate	72
B.5 (a) Layout of a tactile sensor with superstrate and (b) cut-out of the 3-D model.....	73
B.6 Process-file of a tactile sensor with superstrate	73
B.7 Meshed solid model of a tactile sensor with superstrate	74

B.8 Mesher settings.....	75
B.9 MemMech settings.....	75
B.10 MemMech advanced settings	76
B.11 Boundary condition settings.....	76
C.1 Voltage and current characteristics for T1 without superstrate (a) Device # I and (b) Device # II	78
C.2 Voltage and current characteristics for T2 without superstrate (a) Device # I and (b) Device # II	79
C.3 Voltage and current characteristics for T3 without superstrate Device # I	80
C.4 Voltage and current characteristics for T4 without superstrate (a) Device # I and (b) Device # II	81
C.5 Voltage and current characteristics for T1 with superstrate (a) Device # I and (b) Device # II	82
C.6 Voltage and current characteristics for T2 with superstrate Device # I	83
C.7 Voltage and current characteristics for T3 with superstrate (a) Device # I and (b) Device # II	84
C.8 Voltage and current characteristics for T4 with superstrate Device # I	85

LIST OF TABLES

Table	Page
1.1 Design parameters for developing tactile sensors	3
1.2 Comparative study of the specifications of different tactile sensors	4
1.3 Comparative study of different polysilicon-based pressure sensors	5
1.4 Properties of selected polymer materials	7
1.5 Futuristic areas where tactile sensors are needed	14
2.1 Material Properties of the Tactile Sensor	28
2.2 Summary of simulated results for flexible tactile sensors	32
2.3 Summary of simulated results for flexible tactile sensors with superstrate	36
4.1 Results for tactile sensors without superstrate	50
4.2 Results for tactile sensors with superstrate.....	51
4.3 Offset voltage and differential voltage results for devices without a superstrate for 1V input bias voltage	55
4.4 Offset voltage and differential voltage results for devices with a superstrate for 1V input bias voltage	57
A.1 Different pressure sensor designs	66

LIST OF SYMBOLS

SYMBOLS	EXPLANATION	UNITS
A_1, A_2	Active piezoresistors	Ω
$\Delta A_1, \Delta A_2, \Delta P_1, \Delta P_2$	Changes in active and passive piezoresistors	Ω
α_f	Thermal expansion coefficient of the film	$1/^\circ\text{C}$
α_s	Thermal expansion coefficient of the substrate	$1/^\circ\text{C}$
χ	Summation of the Young's moduli of the film and substrate	GPa
d_f	Thickness of the film	μm
d_f^-	Thickness of the deposited film on a compliant substrate	μm
d_s	Thickness of the substrate	μm
d_s^*	Thickness of the compliant substrate	μm
ε	Strain	N/A
ε_{field}	Electric field	V/m
ε_M	Total strain	N/A
ε_{th}	Thermal expansion mismatch strain	N/A
ε_{top}	Top surface strain	N/A
$\varepsilon_{xx}, \varepsilon_{yy}$	Transverse and longitudinal strains in XX and YY directions	N/A

ε_0	Intrinsic strain material	N/A
η	Ratio of the thicknesses of the film and substrate	N/A
γ_{xy}	Shear strain in the XY direction	N/A
i	Current	Amp
ν	Poisson's ratio	N/A
ΔP	Change in Pressure	MPa
P_1, P_2	Passive piezoresistors	Ω
π_{ij}	Piezoresistance coefficients	1/Pa
π_l, π_t	Longitudinal and transverse piezoresistance coefficients	1/Pa
R, R'	Aromatic groups	N/A
$\Delta R/R$	Normalized resistance change	N/A
R_{curv}	Radius of curvature	μm
ρ	Resistivity of a material	$\Omega\text{-m}$
$\Delta\rho_i/\rho_i$	Fractional resistivity change	N/A
$\rho_1, \rho_2, \rho_3, \rho_4, \rho_5, \rho_6$	Resistivities of unstressed isotropic material	$\Omega\text{-m}$
S	Sensitivity	mV/V/MPa
σ	Stress	Pa

σ_f	Internal stress of the deposited film on a compliant substrate	Pa
σ_s	Stress of the compliant substrate	Pa
$\sigma_1, \sigma_2, \sigma_3$	Normal stresses	Pa
σ^*	Uniaxial stress	Pa
ΔT	Change in temperature	°C
τ_1, τ_2, τ_3	Shear stresses	Pa
ΔV	Change in voltage	Volts
V_{in}, V_{out}	Input and output voltages	Volts
V_{input}	Input voltage	Volts
ΔV_{out}	Change in output voltage before and after load application	Volts
Y	Young's modulus	GPa
Y_f	Young's modulus of film	GPa
Y_f^*	Young's modulus of deposited film on a compliant substrate	GPa
Y_s	Young's modulus of substrate	GPa
Y_s^*	Young's modulus of a compliant substrate	GPa
\bar{Y}	Plane strain elastic modulus	GPa

CHAPTER 1
INTRODUCTION
1.1 Background

In the ancient Greek language prosthesis or prosthetic means: “addition”. The prosthetic limb is defined as an artificial extension to a missing part from the human body. These extensions or devices are of different types with their own respective applications and functions (examples: upper and lower-limb prosthetics, heart valves and palatal obturators).

The main focus of this research is towards tactile sensing in upper-limb prosthetics. This area of prosthetics is difficult to treat as there are several technological limitations- primarily lack of sensation (i.e. touch, heat and cold), uncomfortable human-prosthetic limb interfaces and the resemblance of an artificial (or fabricated) limb to a human limb. At present the prosthetic arms in use require and utilize human visual aid to grab or release certain objects. The necessity to sense the forces acting upon these limbs has to be automated to reduce the strain on the user. The idea to obtain tactile sensing was the reason behind developing prosthetic (smart artificial) skin.

The advances in the semiconductor industry to miniaturize devices helped in fabricating tactile microsensors. They are part of microelectromechanical systems (MEMS) which sense the physical stimuli like pressure and force. Recent advances in fabricating MEMS devices on flexible substrates has a greater impact on prosthetic arm applications as it can fit on top of the artificially fabricated arm's non-planar surface [1,2]. The microsensors should have characteristic features like: force sensing range, spatial resolution, response profile, time

resolution, size of the sensing area and substrate flexibility [3]. Furthermore, these microsensors have advanced features: built-in vacuum for absolute pressure measurement, integrated telemetry link, closed-loop control, insensitive to contaminants, ceramic materials to withstand harsh and high-temperatures [4].

Examples of Tactile sensors

The most primitive form of tactile sensors are spatial switches (example of a single binary device). With increase in tactile sensing applications in different research and commercial areas (like medicine, robotics, entertainment, manufacturing and service industries) there was a need to develop advanced sensing devices. These devices can detect stimuli like force, shape of object, size, presence, weight, position, surface texture, hardness. The process of extracting and informing the brain regarding the above stimuli is called haptic perception [5].

This is shown in Fig.1.1.


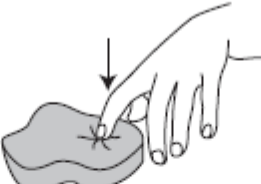

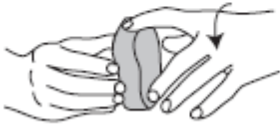
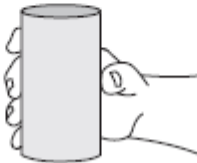

Static contact	Pressure	Lateral motion
 Temperature	 Hardness	 Surface texture
Contour following	Enclosure	Unsupported holding
 Global shape, exact shape	 Global shape, volume	 Weight

Fig. 1.1 Different kinds of haptic perception [5]. Reprinted with permission.

Depending on their design, sensing mechanisms, materials, fabrication techniques and specifications a few are mentioned below-

At the primitive stage of tactile sensing technologies Leon Harmon (in 1982) was the first to extensively work on determining several parameters required to develop these devices. A few specifications for these devices are mentioned below in Table 1.1.

Table 1.1 Design parameters for developing tactile sensors [6]. Reprinted with permission.

Harmon's design criteria	Character
Sensing surface	Compliant and durable
Spatial resolution between sensing points	1 to 2 mm
Number of sensing points in an array	Between 50 and 200
Minimum force sensitivity	1 gram force (0.01 N)
Dynamic range	About 1000:1
Output response	Monotonic, not necessarily linear
Frequency response	At least 100 Hz
Stability and repeatability	Good
Hysteresis	Low

After Harmon, there were several studies on improvising the technology at the sensor level for detecting several stimuli. The following examples for different tactile sensors were reported in between 1990 to 2010: Wolffenbuttel et al. reported on silicon-based piezoresistive and capacitive microsensors which rely on the principle of force sensing elements with diaphragms/cantilevers [7]. Silicon based piezoresistive force sensors by Beebe et al. were shown to measure force applied on the sensor surface. Advantages include linear response, low hysteresis, robust packaging and overload tolerance [8]. Bart et al. demonstrated stress sensor arrays that measure triaxial stress profiles with a high stress resolution and with spatial

resolution comparable to the papillary ridges in the dermis of human skin [9]. Thomas et al. developed a novel contact piezoresistive force sensing mechanism. The device was fabricated using screen-printing technology to deposit semiconductor materials on polyester sheets. Force applied on the sensor sheets resulted in a change in conductance [3]. The specifications for this large area force sensor in comparison with the human skin are shown in Table 1.2.

Table 1.2 Comparative study of the specifications of different tactile sensors [3]. Reprinted with permission.

	Human Skin	Fingerprint Imaging Sensor	Smart Skin
Resolution (mm)	2	0.1	0.1-10
Sensor Area (mm ²)	25x25	13x20	10 ² -10 ⁷
Number of Sensels	10 ²	~10 ⁴	10 ² -10 ⁶
Sensel Force Range (N)	0.4-10	switch	0.05-100
Linearity	Moderate	-	High
Hysteresis	Low	-	Very Low
Compliance	Yes	No	Yes
Bandwidth (Hz)	100	~10	100
Operating Temperature (°C)	-20 to 60	-10 to 45	-40 to 100

Engel et al. developed a polymer based sensor with thin-film metal nichrome (NiCr) as the strain gauge which is considered a step closer to dexterous manipulation and on obtaining information regarding the object in contact with the sensing region. The advantages of this tactile sensor are- robustness, low-cost and flexible substrate [10]. Javey et al. recently developed a mechanically robust, low-voltage consuming artificial electronic skin by contact-printing parallel arrays of semiconductor nanowires to form a flexible pressure-sensor array. The fabricated devices show high-performance, high spatial resolution, low operating voltage and good reliability [11]. Patil et al. presented a study on polysilicon-based pressure sensors for low-pressure applications. The semiconductor (polysilicon) piezoresistor was used as the sensing material. Table 1.3 shows the specifications of different polysilicon-based pressure sensors [12].

Table 1.3 Comparative study of different polysilicon-based pressure sensors [12]

Ref.	Substrate (Micromachining)	Polysilicon Deposition Method	Thickness of Polysilicon Film (nm)	Sensing Area (mm x mm)	Max. Pressure (MPa)	Sensitivity (Kind of Wheatstone Bridge)
[13]	Si (Surface)	LPCVD with phosphorous doping	100	0.1 x 0.1	0.69	21.74 mV/V/MPa (Half)
[14]	Si (Bulk)	LPCVD at 620 °C followed by boron doping, followed by crystallization step at 1100 °C	460	3 x 3	0.02	500 mV/V/MPa (Full)
[15]	Kapton (Surface)	α -Si:H PECVD followed by annealing at 350 °C for 30 minutes	200nm α -Si:H + 65nm n+ α -Si:H	10 x 10	0.014	23.54 mV/(MPa) ^{1/2} (Full)
[16]	Si (Bulk)	LPCVD with boron doping followed by annealing step at 1050 °C	N/A	0.37 x 0.37	1	15.5 mV/V/MPa (Full)
[17]	Si (Bulk)	LPCVD with boron doping	240	1.15 x 1.15	0.15	230 mV/V/MPa (Full)
[18]	Si (Surface)	LPCVD followed by boron doping and annealing at 800 °C for 15 hours	400	0.1 x 0.1	0.7	68.7 m Ω / Ω /MPa
[19]	Si (Bulk)	LPCVD at 625 °C followed by boron doping at 1100 °C	80	2:1 (Ratio)	0.6	15.5 mV/V/MPa (Full)
[12]	Polyimide (Surface)	Aluminum Induced Crystallization 400 °C for 90 minutes	500	0.08 x 0.08	0.02 (AFM) 2 (Load-Cell)	41.12 mV/V/MPa (Half) 5.02 mV/V/MPa (Half)

The goal of this research is to demonstrate the design, fabrication and characterization of tactile sensors. These sensors were then used to develop a prosthetic skin. The project has a greater emphasis on flexible substrates as it lays the foundation for fabricating a prosthetic skin.

1.2 Flexible Substrate

With an increasing demand to improve tactile sensor functionality on robot end-effectors, grippers and manipulators in the industrial and medical sectors, researchers have searched for several options. The major problem they had to face was due to fabrication on rigid silicon substrates whereas the end goal was to mount these devices on robotic or functioning artificial arms which have curved surfaces. After considerable efforts they had opted to use flexible substrates which had a better future in this particular area. Although sensors fabricated on rigid silicon substrates have proven to be commercially successful they have a major limitation of being mechanically brittle. Moreover, they lack the suppleness and compliance hindering these devices from undergoing large deformations and impacts. On the other hand, flexible substrates provided an apt solution as they have a higher degree of conformity to the artificial arms. With this distinct change, the material requirements, manufacturing techniques, applications changed drastically. A whole new set of modified fabricating techniques (processing steps like imaging, etching, plating, die cutting and assembly) were developed. The potential areas in which these types of devices can be used are- prosthetic devices, conformal sensor arrays, electronic fabrics and smart tags. The primary advantages being: can cover large areas of non-conformal surface contours, light-weight, cost-effectiveness, compliancy and volume efficiency [20]. The figure below depicts tactile sensors fabricated on a flexible substrate.



Fig. 1.2 Tactile sensors on a flexible substrate

Flexible substrates should have characteristic properties such as: chemical inertness, high elastic modulus, dielectric (or electrically insulating characteristics) and thermal stability [21]. The Table 1.4 shows several properties to be considered when choosing the right polymer material for the flexible tactile sensor fabrication.

Table 1.4 Properties of selected polymer materials [4]

	EPON SU-8	Parylene	PDMS	Polyimide
Dielectric constant (60 Hz)	5.07	2.65-3.15	2.7	3.5
Dissipation factor (60 Hz)	0.007	0.02-0.0002	0.001	0.002
Moisture absorption (%)	N/A	0.01-0.06	0.1	2.8
Glass transition temperature (°C)	194	160	-125	360-410
Coefficient of thermal expansion (ppm/°C)	20-50	35-69	30	20
Tensile strength (MPa)	50	45-75	6.2	200-234
Tensile modulus (GPa)	4-5	2.4-3.2	0.0005-0.001	2.5-4
Elongation at break (%)	< 1	10-200	100	10-150
Density (g/cm ³)	1.2	1.1-1.4	1.05	1.42-1.53
Representative patterning methods	Photo definition, plasma etch	Plasma etch	Molding, plasma etch (slow)	Photo definition, wet etch, plasma etch
Reference	Resolution Performance Products, LLC	Parylene Coating Services Inc.	Dow Corning, Inc.	Kapton, Dupont

From Table 1.4, it can be seen that polyimide shows outstanding electrical insulation, thermal stability (up to 400°C), mechanical robustness and durability compared to other polymer materials (the reason it being used predominantly in the microelectronic industry).

Polyimide films are formed from a condensation polymer consisting of an aromatic dianhydride and an aromatic diamine forming cyclic polymers consisting of aromatic groups R and R'. Aromatic groups (examples: ether, carbonyl) are incorporated in the polyimide during condensation to change the polymer properties. By the addition of these groups the film forming

ability, glass transition temperature, inherent viscosity and thermal stability of the polymer can be varied. In addition, it can be used to pattern features or it is photo-definable by chemically altering the aromatic groups. Compared to the other thermosetting polymers, polyimide films are highly flexible. One main disadvantage is that their moisture absorption is around 3% water by weight causing blistering and delamination. This can be solved by dehydrating the film before further processing.

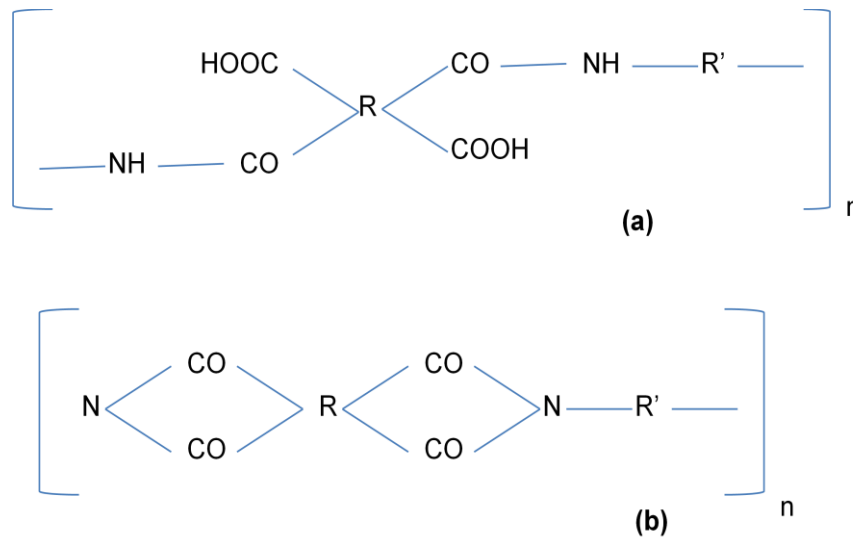


Fig. 1.3 Polyimide: polymer structure. (a) Generic polyamic acid (b) polyimide after imidization reaction [4]

Commercially available polyimide films are made to have similar thermal expansion rates as of metals and ceramics. The above properties make it possible to structurally integrate polyimide in tactile sensors [4,20].

In order to understand the mechanical behavior of flexible substrates one should understand the theory behind the mechanical stresses that are introduced when they undergo deformation. The internal factors to be considered: built-in stress during film growth (or intrinsic stress), mismatch of coefficient of thermal expansion between layers (or residual stress) and humidity intake. To realize the mechanics of these substrates consisting of the device, sacrificial and passivation layers, we assume that the device-level film is a continuous homogenous film

on top of a polymer substrate. This simplification gives the basic idea as to how flexible substrates behave. The difference in the thermal expansion coefficients of silicon and flexible substrate results in the warping of the rigid substrate [22]. Fabrication processes for compliant substrates have to be implemented by bonding them on to a rigid carrier wafer (glass, oxidized or nitrated silicon wafer) so as to use conventional planar semiconductor fabrication techniques. The value of stress is given by:

$$\sigma = Y\varepsilon \quad (1.1)$$

Y is the Young's or elastic modulus followed by the strain which is given as ε . Important factors which determine the behavior of the film-on-substrate are Young's modulus and thickness of the substrate and film- Y_s, d_s, Y_f, d_f . For tactile sensors, the assumption made here is to have similar products of Young's modulus and thickness $Y_f d_f^2 \approx Y_s d_s^2$ as the model to be considered has a homogeneous stiff film and compliant substrate [22]. Now to determine the values of stress, strain and radius of curvature of the model the expressions are as follows.

The total strain in the model can be determined by the summation of the intrinsic and the residual strains that arise due to processing of the films and the thermal mismatch between the layers.

$$\varepsilon_M = \varepsilon_0 + \varepsilon_{th} \quad (1.2)$$

wherein, $\varepsilon_M, \varepsilon_0, \varepsilon_{th}$ are the total strain, built-in or intrinsic and thermal expansion or residual strain mismatches, respectively. Therefore:

$$\varepsilon_{th} = (\alpha_f - \alpha_s)\Delta T \quad (1.3)$$

The thermal expansion mismatch strain, ε_{th} is defined as the product of the difference between thermal expansion coefficients of the film and substrate (i.e. α_f and α_s) and the temperature change, ΔT [22].

To understand the mechanical behavior of the homogeneous thin film with respect to a compliant or flexible substrate the following assumptions are made.

When a film is deposited on a compliant substrate the film's internal stress is given as:

$$\sigma_f = \left[\frac{\varepsilon M Y_f^*}{1 + Y_f^* d_f / Y_s^* d_s} \right] \quad (1.4)$$

In the Eq. (1.4) Y_f^*, Y_s^* and d_f^*, d_s^* are the Young's moduli and the thicknesses of the deposited film and flexible substrate. The film stress obtained from the equation is now reduced by half because of its dependence on the substrate's thickness and Young's modulus [22]. The compliant substrate stress is given as,

$$\sigma_s = \left[-\sigma_f d_f / d_s \right] \quad (1.5)$$

Eq. (1.5) shows that the value of stress is very small compared to that of the film as it is dependent on the thickness of the layers. The radius of curvature (R_{curv}) is determined by:

$$R_{curv} = \left[\frac{(\bar{Y}_s d_s^2 - \bar{Y}_f d_f^2)^2 + 4\bar{Y}_s \bar{Y}_f d_f d_s (d_f + d_s)^2}{6\varepsilon(1+\nu)\bar{Y}_s d_f d_s (d_f + d_s)} \right] \quad (1.6)$$

From the above expression \bar{Y} is the plane strain elastic modulus and ν is the Poisson's ratio.

The flexible substrate with the devices on top rolls up in to a cylinder when it is peeled off a rigid frame. Similarly, when the compliant sheet is bent, we can calculate the strain on the top surface of the film. Upon bending the sheet, the top surface has tensile stress and the bottom surface has compressive stress (Fig. 1.4). Therefore, there is a neutral plane in which the strain values are zero [22].

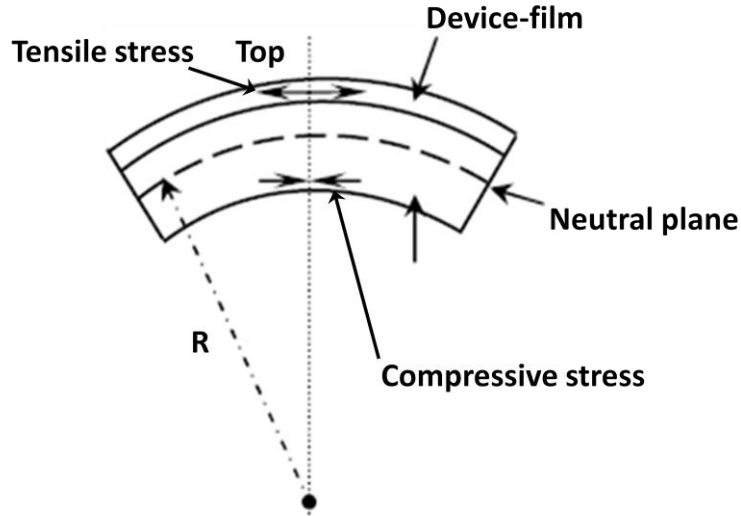


Fig. 1.4 Device-film on a compliant substrate depicting the stresses, neutral plane and radius of curvature [22]

The expression used to measure the top surface strain, ϵ_{top} for a stiff substrate is

$$\epsilon_{top} = \left[(d_f + d_s) / 2R_{curv} \right] \quad (1.7)$$

ϵ_{top} for a compliant substrate is given as:

$$\epsilon_{top} = \left[\frac{(d_f + d_s)}{2R_{curv}} \frac{1 + 2\eta + \chi\eta^2}{(1 + \eta)(1 + \chi\eta)} \right] \quad (1.8)$$

From the above equation the values of $\eta = d_f / d_s$ and $\chi = Y_f + Y_s$. Hereby, we can determine that the strain on the top is reduced by a considerable amount. To further decrease the strain on the top surface, a superstrate can be bonded on the film [22]. The material considerations and mechanics of utilizing a superstrate will be explained in the following chapters.

1.3 Tactile sensors

A tactile sensor can be defined as a transducer that can detect and quantify the property of an object in contact, simultaneously convert and process the information obtained.

The development of the tactile sensor for upper-limb prosthetics in this research was primarily based on piezoresistive pressure sensors. This particular section is on pressure sensors. These devices are widely used in the MEMS industry because they are cost-effective, high-performance and enable varied applications (examples: intravenous blood pressure measurement, automobile manifold air and tire pressure, industrial process control, hydraulic systems and microphones). The block diagram in Fig. 1.5 explains the basic components of a pressure sensor, where upon pressure application, the sensing element undergoes a change in shape resulting in strain formation in the material used for analyzing the magnitude of pressure.

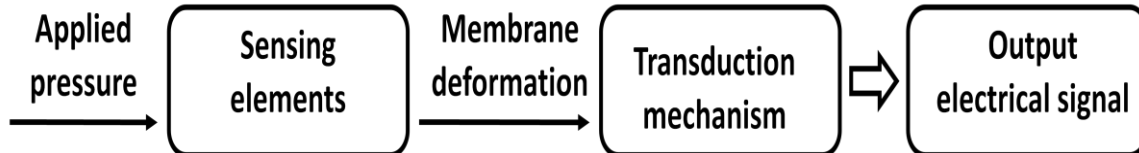


Fig. 1.5 Basic components of a pressure sensor [23]

Fundamentally there are three types of pressure sensors:

1. Absolute pressure sensors: The pressure is measured relative to a known pressure. Used to measure the pressure in internal combustion chambers in automobiles, as an example.
2. Gauge pressure sensors: The pressure is measured relative to atmospheric pressure. Used to obtain blood pressure measurements, as an example.
3. Differential pressure sensors: The measured pressure is the difference of two pressures applied to the sensing area [23].

Several different pressure sensors have been developed for a wide range of pressure-sensing applications.

The ideal pressure sensor would have the following features:

1. Linearity: For a sensor linear response to pressure over its entire operating range is preferable. MEMS pressure sensors are based on micromachined diaphragms wherein the sensor output shows a declining rate for an increasing applied pressure [24].
2. Zero/offset: The sensor output with a zero applied pressure and at constant temperature is called zero/offset.
3. Hysteresis: The measure of the repeatability of a sensor's output against the operating pressure range over many cycles. The sensor output when undergoing loading (pressure increases from zero to full scale) and unloading (pressure falls from full scale to zero) is different.
4. Long-term drift: The change in the sensor output over time is measured as the long-term drift. This drift occurs over a period of time because of pressure cycling, temperature changes and sensor mounting problems [23].

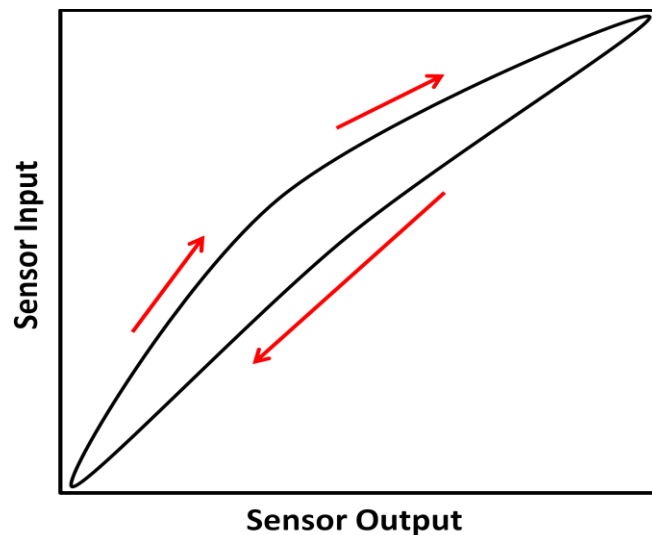


Fig. 1.6 Hysteresis: sensor input vs. sensor output [23]

5. Sensitivity (S): The ratio of the relative difference in the output voltage to the change in applied pressure. Sensitivity is determined by calculating the aforementioned ratio to the specified input voltage:

$$S = \frac{\Delta V}{\Delta P} \frac{1}{V_{input}} \quad (1.9)$$

6. Effect of temperature: The sensor performance suffers from several negative effects as it undergoes temperature cycling. Span temperature hysteresis is the difference of the span readings after minimum and maximum operating temperatures are applied.

The efforts to develop the MEMS pressure sensors have led the way to new sensing and micromachining techniques. The most commonly used are piezoresistive, capacitive and resonant pressure sensors. Other sensing techniques include:

- Surface acoustic wave (SAW) resonators in which interdigital transducers (IDT) are used to detect the pressure. Piezoelectric substrates like quartz are used in these devices.
- Optical techniques utilize the elasto-optic effect wherein a deformation of the sensor membrane causes a change in the phase of an incident light wave.
- Inductive coupling has two planar coils that are fabricated above and below the membrane structure and upon application of an alternating current (AC) to the above coil, the pressure variations on the membrane are detected by the change in induced current of the lower coil [23,24].

With the above mentioned sensing techniques these sensors can be successfully implemented to meet current and future needs in specific areas (shown in Table 1.5).

Table 1.5 Needs in specific market sectors where tactile sensors are needed [6]. Reprinted with permission.

Surgery and Medicine	
Feature	Need
Very rapid take-up	Restore taction in minimal invasive surgery
Disposable equipment	Laparoscopy improvements
Sophisticated users	Remote palpation
Technical issue	Challenge
Telepresence	Force and tactile feedback
Teletaction	Mobility, fine control
Soft tissue discrimination	Hardness/softness sensing

Table 1.5 - continued

Health Care and Service Robotics	
Feature	Need
Demographic projections	Personal space manipulation
Enormous demand imminent	Mobility aids
Cost reduction essential	Automated household tools
Technical issue	Challenge
Haptic exploration, dexterity	Safety
Adaptation, customization	Reliability
Low costs	User acceptance
Natural Product Processing	
Feature	Need
High volume	High speed
Human excluded environment	Inspection function
Versatile, product changes	Consistency
Technical issue	Challenge
Soft, delicate items	Active handling control
Irregular objects	Reliability
Long run-times	Hygiene

The working principle of piezoresistive pressure sensors are addressed in detail in Chapter 2. As piezoresistivity is one of the many types of sensing mechanisms used in MEMS sensors it is widely used in accelerometers, flow sensors, gyro-rotation rate sensors, chemical sensors, pressure sensors and tactile sensors among several others.

1.4 Piezoresistivity

Piezoresistive effect was first discovered by Lord Kelvin in the year 1856. This is a material property exhibited by most materials (examples: metals, semiconductors, conductive elastomers and carbon fibers). Change in resistivity of a semiconductor material due applied mechanical stress is known as piezoresistivity. The first experimental results were made by Smith [25] and Adams [26] from Bell Labs in 1954 on silicon and germanium. The piezoresistive effect of both metals and semiconductors were shown by several researchers: Reilly et al., Hu et al. and Barlian et al. [27-29]. At a microscopic level the piezoresistive effect can be explained differently in metals and semiconductors. In metals, the highest filled level occurs at a mid-band gap range, which results in several empty states having similar energies to the highest filled

bands. The application of stresses on the material causes change in the inter-atomic positions resulting in slightly distorted energy bands. This results in a small change in conduction due to the applied electric field. In semiconductors, the highest filled level is at the edge of the valence band in which case the conduction band remains empty. In thermal equilibrium the conduction band and valence band have some electrons and holes respectively. The application of stresses on the semiconducting material causes change in the inter-atomic positions resulting in small changes in the band-edge energies [4,30,31,32].

The mathematical model for piezoresistivity can be explained by a three-dimensional relationship of the current (i) and electric field (ε_{field}). These two factors are related to an anisotropic and symmetric crystal by a three-by-three resistivity tensor matrix. A symmetric crystal follows the expression:

$$\begin{bmatrix} \varepsilon_1 \\ \varepsilon_2 \\ \varepsilon_3 \end{bmatrix} = \begin{bmatrix} \rho_1 & \rho_6 & \rho_5 \\ \rho_6 & \rho_2 & \rho_4 \\ \rho_5 & \rho_4 & \rho_3 \end{bmatrix} \begin{bmatrix} i_1 \\ i_2 \\ i_3 \end{bmatrix} \quad (2.0)$$

where ρ_1 to ρ_6 are the resistivities of the unstressed isotropic material. For an isotropic material, the values in the above equation become $\rho_1 = \rho_2 = \rho_3 = \rho$ and $\rho_4 = \rho_5 = \rho_6 = 0$. Eq. (2.0) is for an unstressed symmetric crystal. In this particular case, as the material is a piezoresistor, the six resistivity components are stress dependent. The breakup of these individual stresses can be shown by a cube of infinitesimal dimensions dx, dy and dz [33]. The six components can be further divided in to three normal: $\sigma_1, \sigma_2, \sigma_3$ and three shear τ_1, τ_2, τ_3 stresses.

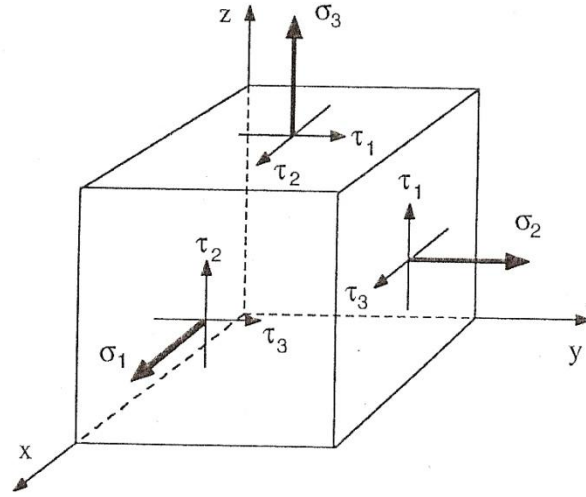


Fig. 1.7 Representation of normal and shear stresses [33]. Reprinted with permission.

The equation for an isotropic material stressed condition:

$$\begin{bmatrix} \rho_1 \\ \rho_2 \\ \rho_3 \\ \rho_4 \\ \rho_5 \\ \rho_6 \end{bmatrix} = \begin{bmatrix} \rho \\ \rho \\ \rho \\ 0 \\ 0 \\ 0 \end{bmatrix} + \begin{bmatrix} \Delta\rho_1 \\ \Delta\rho_2 \\ \Delta\rho_3 \\ \Delta\rho_4 \\ \Delta\rho_5 \\ \Delta\rho_6 \end{bmatrix} \quad (2.1)$$

The fractional resistivity change $\Delta\rho_i/\rho_i$ can be related to the stress components which yield a matrix with 36 coefficients (also called piezoresistance coefficients, π_{ij}). The units in which π_{ij} can be expressed are in Pa^{-1} . The matrix formed is:

$$\frac{1}{\rho} \begin{bmatrix} \Delta\rho_1 \\ \Delta\rho_2 \\ \Delta\rho_3 \\ \Delta\rho_4 \\ \Delta\rho_5 \\ \Delta\rho_6 \end{bmatrix} = \begin{bmatrix} \pi_{11} & \pi_{12} & \pi_{12} & 0 & 0 & 0 \\ \pi_{12} & \pi_{11} & \pi_{12} & 0 & 0 & 0 \\ \pi_{12} & \pi_{12} & \pi_{11} & 0 & 0 & 0 \\ 0 & 0 & 0 & \pi_{44} & 0 & 0 \\ 0 & 0 & 0 & 0 & \pi_{44} & 0 \\ 0 & 0 & 0 & 0 & 0 & \pi_{44} \end{bmatrix} \begin{bmatrix} \sigma_1 \\ \sigma_2 \\ \sigma_3 \\ \tau_1 \\ \tau_2 \\ \tau_3 \end{bmatrix} \quad (2.2)$$

Eq. 2.2 depicts the properties of a crystalline material (example: silicon and germanium). As the crystal is assumed to be an isotropic material this matrix is invariant under symmetry operations of the crystal lattice. Upon simplification of this matrix under symmetry conditions three different piezoresistive coefficients remain: $\pi_{11}, \pi_{12}, \pi_{44}$. The electric field in a cubic crystal under stressed conditions can be obtained from solving Eqs. 2.0, 2.1 and 2.2:

$$\begin{aligned}\varepsilon_1 &= \rho i_1 + \rho \pi_{11} \sigma_1 i_1 + \rho \pi_{12} (\sigma_2 + \sigma_3) i_1 + \rho \pi_{44} (i_2 \tau_3 + i_3 \tau_2) \\ \varepsilon_2 &= \rho i_2 + \rho \pi_{11} \sigma_2 i_2 + \rho \pi_{12} (\sigma_1 + \sigma_3) i_2 + \rho \pi_{44} (i_1 \tau_3 + i_3 \tau_1) \\ \varepsilon_3 &= \rho i_3 + \rho \pi_{11} \sigma_3 i_3 + \rho \pi_{12} (\sigma_1 + \sigma_2) i_3 + \rho \pi_{44} (i_1 \tau_2 + i_2 \tau_1)\end{aligned}\quad (2.3)$$

The first and second terms in Eq. 2.3 relate to the unstressed conduction and the piezoresistance effect in the cubic crystal. Remaining terms define the complicated behavior of the crystal lattice under stress and are material-dependant properties [33].

In order to obtain the piezoresistive properties in an arbitrary Cartesian system the axes have to be transformed to a local co-ordinate system. Two types of piezoresistance coefficients are considered in sensors: longitudinal and transverse. When the stress applied is along the direction of the current (i^*) and electric field (ε^*), the longitudinal piezoresistance coefficient (π_l) is given by:

$$\pi_l = \pi_{11} + 2(\pi_{44} + \pi_{12} - \pi_{11})(l_1^2 m_1^2 + l_1^2 n_1^2 + m_1^2 n_1^2) \quad (2.4)$$

Likewise, when the stress applied is normal to the current (i^*) and electric field (ε^*), transverse piezoresistance coefficient (π_t) can be written as:

$$\pi_t = \pi_{12} - (\pi_{44} + \pi_{12} - \pi_{11})(l_1^2 l_2^2 + m_1^2 m_2^2 + n_1^2 n_2^2) \quad (2.5)$$

The schematic representation for the above two types of piezoresistance coefficients are shown in the following Fig. 1.8 [33].

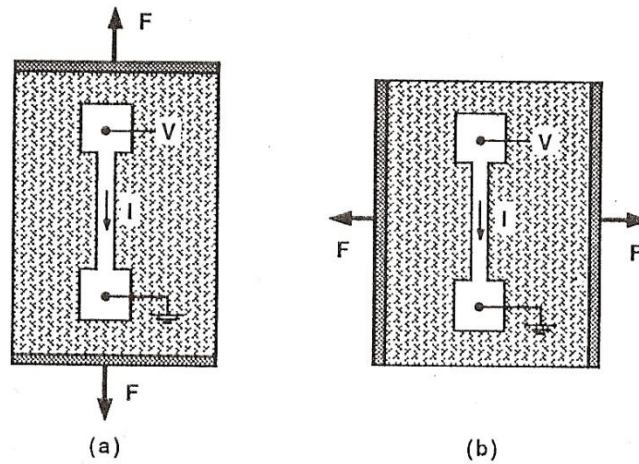


Fig. 1.8 a) Longitudinal piezoresistance coefficient (b) transverse piezoresistive coefficient cases [33]. Reprinted with permission.

Metal resistors have been used for various commercial applications such as pressure gages, flow meters and displacement transducers. The main criteria to choose a piezoresistive material are good Gauge factor (GF), great thermal and temporal stability, low temperature coefficient of resistance (TCR) and low thermo-electric power (TEP). Thin films in general have characteristic features like high sheet resistance and high GF's in comparison to their bulk counterparts. Reproducibility and temporal stability also play a vital role if the thin films are discontinuous. Such films are not good for device applications. The GF of semiconductors is greater than metals. Semiconducting piezoresistive materials are not viable because they have a high negative TCR. On the other hand, composite materials made of processed ceramic particles and metals known as cermets also display high GF but cannot be used in devices as they have a very high positive TCR. Both semiconductors and cermets need to have temperature compensation circuitry for practical utilization [34]. Another advantage is the low processing temperature required to deposit metal piezoresistors. Mechanically metal films have a greater sustenance when elongated before they fracture and are therefore used on polymer MEMS tactile sensors [35]. Several research groups have worked on understanding the

electro-mechanical properties of thin film nichrome (Ni-Cr 80/20 wt. %) and have investigated: variation of GF with respect to film thickness [36], measured low TCR [37] and the application of these thin film resistors in fabricating strain-sensitive gauges [38].

1.5 MEMS Packaging

The microelectronics or integrated circuit (IC) packaging industry is relatively old and mature compared to MEMS packaging. A few reasons worth mentioning in regards to IC packaging are: abundance of industrial infrastructure, wide application base and greater understanding of failure mechanisms compared to the MEMS packaging industry, which is relatively at its infancy. Packaging is meant to provide efficient thermal dissipation, mechanical strength to the die, protect against harsh environments and house reliable interconnections to facilitate a varied range of electrical signals. In the case of MEMS devices there are no standardized packaging techniques. Furthermore, there are several diverse parameters to be taken into account which makes it far more complex to achieve good packaging. Broadly, the functionality of a MEMS package can be summarized as below:

- Protection of the micromachined parts depending on the requirement should/ should not provide access to the environment for measuring both physical, biological and chemical parameters.
- Package should be compatible to both the MEMS device and the signal conditioning circuitry.
- Package should provide interconnections to electrical signals and fluid channels [39]

As the MEMS packaging industry is majorly application centric it has several key factors to be considered:

1. Wafer stack thickness
2. Wafer dicing (before and after packaging)

3. Thermal management
4. Special consideration for piezoresistive or piezoelectric materials from undesirable mechanical stresses
5. Protective coating of Parylene or Silicon Carbide protect the package from harsh environments [39]

A brief look at the failure mechanisms for MEMS packages can help assess the quality and reliability. The main factors are:

- Delamination is observed due to the bond failure between similar or dissimilar materials.
- Failure by stiction and wear: Stiction is the microscopic adhesion of two surfaces in contact with each other and wear is due to particulate entrapment hindering the movement of parts.
- Environmentally induced failures: Humidity, shock, vibration, thermal cycling cause failures to the mechanical moving parts.
- Cyclic mechanical fatigue: Materials subjected to cyclic loading see degradation in their mechanical properties. Usually seen in membrane and comb like structures.
- Dampening effect is seen MEMS devices with moving parts. The movement is obstructed because of presence of sealant gases in the packages. This effect can be resolved by gettering.
- Hermeticity: Outgassing of gaseous species from materials causes loss of hermeticity. It can be fixed by right choice of package materials, pre-treatments and gettering [40]

CHAPTER 2

DESIGN AND SIMULATION OF TACTILE SENSORS

2.1 Piezoresistive Pressure Sensor: Theory of Operation

The MEMS piezoresistive pressure sensors presented in this thesis are made up of a membrane (or diaphragm) region and piezoresistors (or sensing elements) connected in a half-Wheatstone bridge configuration. Upon stress application on the membrane (which acts like a stress amplifier) the piezoresistors undergo deformation causing a change in their resistances. A limitation for this type of a sensor is its temperature sensitivity [41], for which a Wheatstone bridge is implemented. The change in the resistance of the sensing element is directly read in the form of a differential voltage.

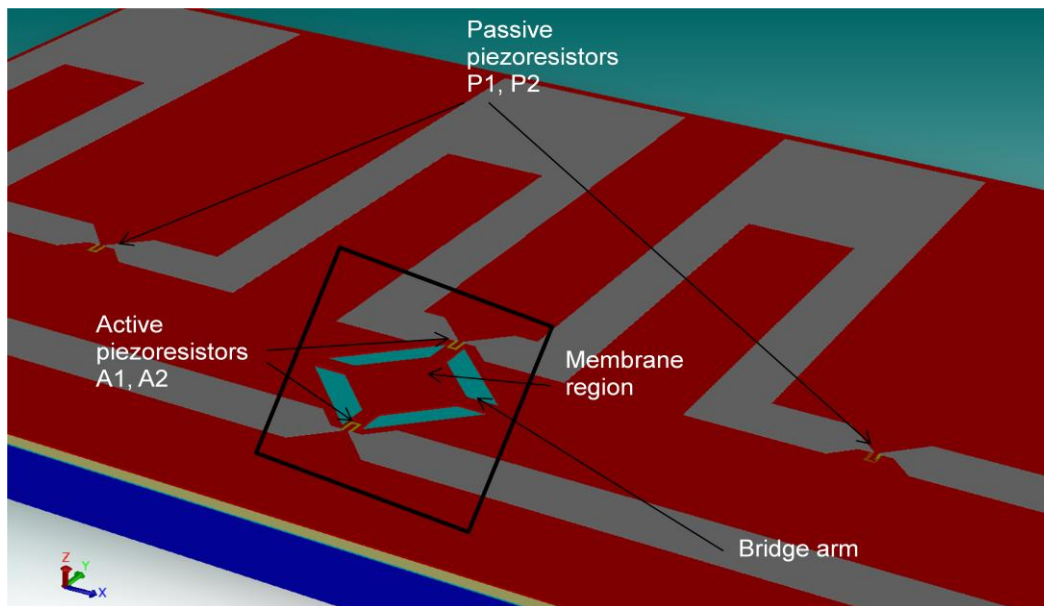


Fig. 2.1 Solid model of the piezoresistive pressure sensor

2.2 Wheatstone Bridge

To understand the operation of the pressure sensor, it is vital to understand the functioning of a Wheatstone bridge. The bridge consists of four piezoresistors- A_1, A_2, P_1 and P_2 . As the sensor is fabricated to have a half-Wheatstone bridge, there are two active piezoresistors: A_1, A_2 and two passive piezoresistors: P_1, P_2 . This configuration is shown in the Fig. 2.2.

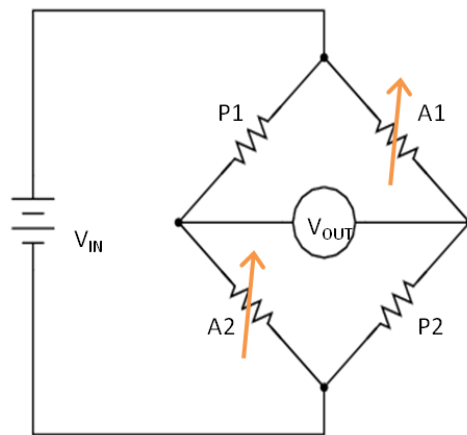


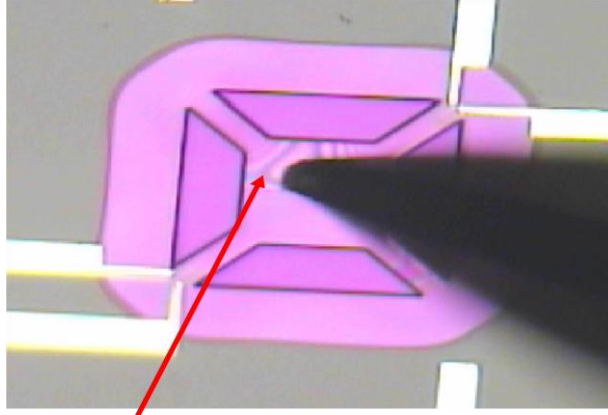
Fig. 2.2 Wheatstone bridge circuit diagram

For a given input bias voltage (V_{in}), the output voltage (V_{out}) can be obtained as:

$$V_{out} = \frac{A_1 A_2 - P_1 P_2}{(A_1 + P_1)(A_2 + P_2)} V_{in} \quad (2.1)$$

Ideally for the bridge to be balanced, the values of the resistors should be equal to obtain an output voltage of zero ($V_{out} = 0$). However, if the resistance values are not exactly equal, one would see a finite output voltage known as the offset voltage. This is termed as an unbalanced bridge.

As mentioned earlier the pressure sensor's membrane is deformed when load is applied. The membrane thus behaves like a stress amplifier. In practice the load application can be depicted by Fig. 2.3.



Strain Contours

Fig. 2.3 Image of the membrane when the load is being applied using a probe-tip

After load application, the output voltage can be given as:

$$V_{out} + \Delta V_{out} = \frac{(A_1 + \Delta A_1)(A_2 + \Delta A_2) - (P_1 + \Delta P_1)(P_2 + \Delta P_2)}{(A_1 + \Delta A_1 + P_1 + \Delta P_1)(A_2 + \Delta A_2 + P_2 + \Delta P_2)} V_{in} \quad (2.2)$$

where $\Delta A_1, \Delta A_2, \Delta P_1, \Delta P_2$ and ΔV_{out} are changes in the resistors A_1, A_2, P_1, P_2 and change in the output voltage.

From Fig. 2.1 and Fig. 2.3 we can see that the membrane region is a corrugated diaphragm. The active piezoresistors A_1 and A_2 are placed on the bridge arms of this region. Upon application of load we can see that the diaphragm undergoes a deformation which in turn is detected by the sensing elements (A_1 and A_2) on the bridge arms. Therefore, it is called the active region. The passive piezoresistors (P_1 and P_2) are located away from the active region because of which they are unaffected by the applied stress, $\Delta P_1 = \Delta P_2 = 0$. Thus,

$$V_{out} + \Delta V_{out} = \frac{(A_1 + \Delta A_1)(A_2 + \Delta A_2) - (P_1 P_2)}{(A_1 + \Delta A_1 + P_1)(A_2 + \Delta A_2 + P_2)} V_{in} \quad (2.3)$$

If all the four resistors and their respective changes in the resistors are equal, then Eq. 2.3 can be simplified to:

$$\Delta V_{out} = \frac{\left(\frac{\Delta R}{R}\right)}{\left(2 + \frac{\Delta R}{R}\right)} V_{in} \quad (2.4)$$

Here, $\Delta R/R$ is the normalized resistance change. For calculating $\Delta R/R$, MATLAB™ was used in which the values of all four pseudo resistances: A_1, A_2, P_1 and P_2 (defined in Chapter 4), V_{in} ($= 1V$), V_{out} and ΔV_{out} are required. The code used to measure the individual resistance values, $\Delta R/R$, $\Delta R/R\%$ and theoretical offset voltage (for verifying the experimentally obtained offset voltage) is presented in APPENDIX B.

The gauge factor (GF) is calculated by obtaining the strain values from the piezoresistor (which are deformed upon load application). The stress analysis cannot be quantified accurately by using conventional methods which use close-form solutions. Credible results for the strain values on the piezoresistors can be extracted by utilizing finite element method (FEM) [42].

In order to calculate the average strain on the piezoresistors with different shapes (U and Y respectively) the areas have to be divided into regions. For a U-shaped, the piezoresistor is divided into three regions and for a Y-shaped it is divided into five regions (shown in Fig. B.1). This helps to calculate the transverse (ε_{xx}) and longitudinal (ε_{yy}) strains. Axis transformation is required to obtain the strain value for a Y-shaped piezoresistor which is given by:

$$\varepsilon_x = \varepsilon_{xx} \cos^2 \theta + \varepsilon_{yy} \sin^2 \theta + \gamma_{xy} \sin \theta \cos \theta \quad (2.4)$$

The values for transverse (ε_{xx}), longitudinal (ε_{yy}), shear (γ_{xy}) strains and angle θ (angle between the global axis and the transferred axis) are used.

From the above values, the average strain can be obtained as:

$$Strain_{AVG} = \frac{Strain_{total}}{Area_{total}} = \frac{\iint [\varepsilon_{xx} + \varepsilon_{yy}] dx dy}{\iint dx dy} \quad (2.5)$$

The values for total strain ($Strain_{total}$) and total area ($Area_{total}$) are obtained by integrating the transverse (ε_{xx}) and longitudinal (ε_{yy}) strains for each individual area of the piezoresistor. $Area_{total}$ is given by integrating the areas of all the regions of a piezoresistor. The total area varies depending on whether it is a U-shaped or Y-shaped piezoresistor. The strain values extracted from the FEA results are formatted in excel files to obtain the total strain and total area using a MATLAB™ code mentioned in APPENDIX B.

The GF for a material can be determined by the obtained values of average strain and $\Delta R/R$. Therefore,

$$GF = \frac{\left(\frac{\Delta R}{R} \right)}{Strain_{AVG}} \quad (2.5)$$

2.3 Design of Flexible Tactile Sensors

Coventorware™ has been used to design the piezoresistive pressure sensors. The two-dimensional layouts of the sensors were used to obtain the solid models (or three dimensional device structures). The design and layout of the device masks was done by Gonenli et al. [43]. The layout was made for ten different devices and consists of five different masks. The devices vary in terms of their membrane dimensions, bridge arm dimensions, piezoresistor shapes and sizes. The two active piezoresistors are placed on two opposite facing bridge arms in a half-Wheatstone bridge configuration. The membrane structure is suspended over the sacrificial polyimide because of isotropic ashing during the fabrication process. The undercut length is

crucial as it decides the boundary conditions for simulating the device structures. The five different mask layouts used in the design of the sensors are presented in APPENDIX A.

2.4 Simulation of Flexible Tactile Sensors

The CAD/ EDA tool used for simulating the devices was CoventorWare™. One of the important factors to be considered before simulating the 3-D tactile sensor model is verifying the geometrical dimensions of the membrane and undercut region of the fabricated device. The undercut for the 3-D model was made to emulate that of the ashed sacrificial polyimide layer beneath the membrane (shown in Fig. B.5).

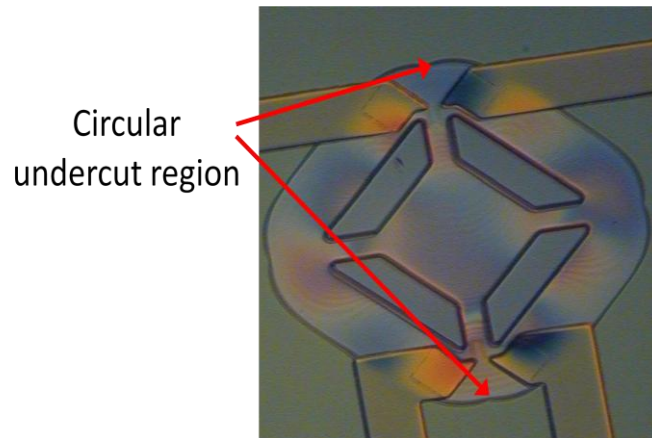


Fig. 2.4 Image of the circular undercut region in a fabricated tactile sensor

The mechanical deformation of the membrane and the piezoresistors can be solved using finite element analysis only if the material properties are given to the analyzer. Table 2.1 presents the material characteristics: Young's modulus and Poisson's ratio utilized for obtaining the displacement magnitude and stress values. The materials were chosen to have linear, elastic and isotropic characteristics. Aluminium oxide was selected for the membrane layer as it is a high performance ceramic material with properties of high hardness, excellent dielectric and good thermal properties. Thin film nichrome alloy (80-20 wt. %) was chosen to study the piezoresistive properties. Aluminium was preferred for metal interconnects as it has very low

electrical resistivity. Polyimide is used as the flexible polymer substrate and superstrate to house the tactile sensors.

Table 2.1 Material Properties of the Tactile Sensor [44-49]

Material	Young's Modulus (GPa)	Poisson's Ratio
Silicon Nitride	304	0.24
Polyimide	7.5	0.35
Alumina	440	0.25
Nichrome	18.6	0.38
Aluminium	30	0.33

Followed by the material properties the boundary conditions play a vital role in deciding the accuracy of the simulated results. The tactile sensors were simulated with the presence of a membrane layer, two active piezoresistors, ashed sacrificial polyimide layer and a patch layer. As a point or area cannot be defined for load application on the surface of a structure in the solid modeler of CoventorWare™ a separate layer was embedded. This embedded layer is in the shape of a disc and it represents the lateral dimension (or diameter) of a probe tip. The probe-tip diameter used for all the experiments in this thesis is 20 μm. The optimum z-thickness of the patch has been set to 0.1 μm. Fig. 2.5 shows the clipped structure of the device undercut region.

Figs. 2.6 and 2.7 depict the conditions used for simulating the mechanical deformations. The settings for simulating the device have been described in APPENDIX B. The results obtained from the simulations have been consolidated and presented in Table 2.2. The simulated results are for four different sensor designs T1, T2, T3 and T4 respectively. The maximum stresses can viewed from the simulated results. Figs. 2.8 and 2.9 show the Mises stress for sensor designs T2 and T4.

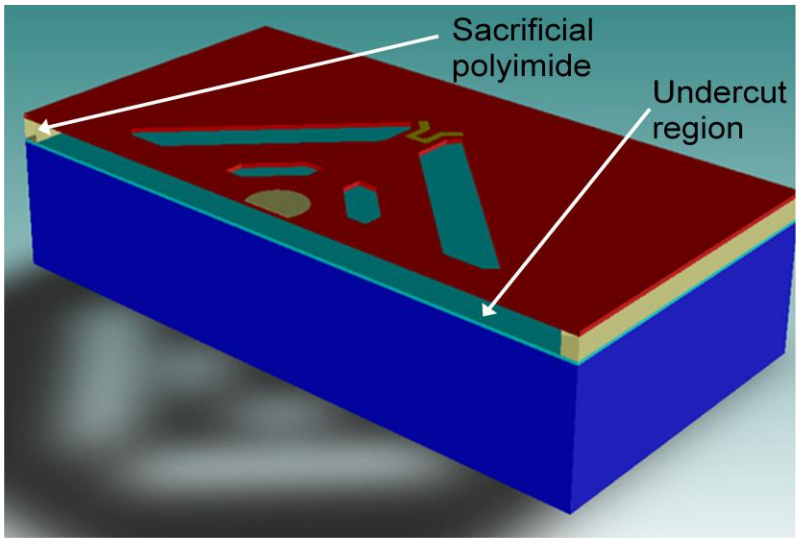


Fig. 2.5 Clipped structure of the simulated tactile sensor

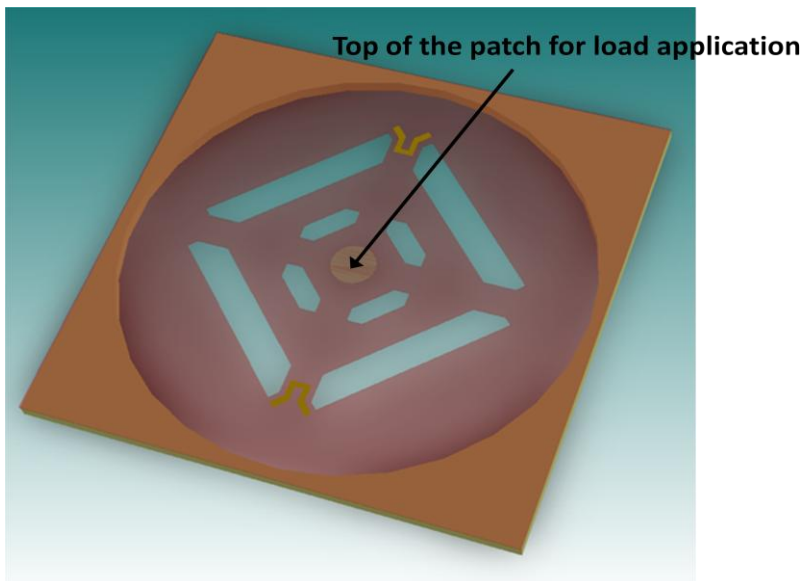


Fig. 2.6 Load application on the 20 μm patch

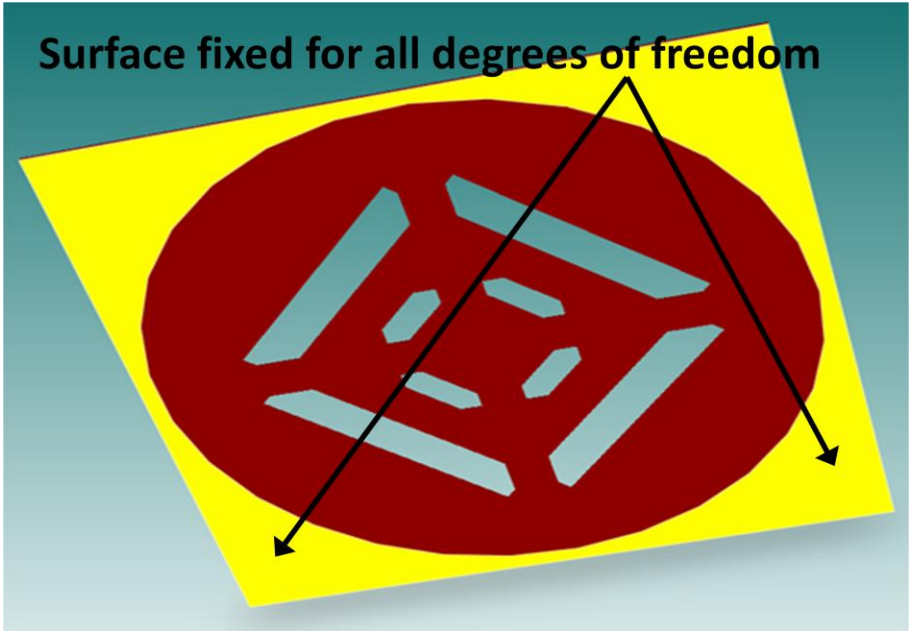


Fig. 2.7 Boundary conditions emulating the ashed sacrificial polyimide layer

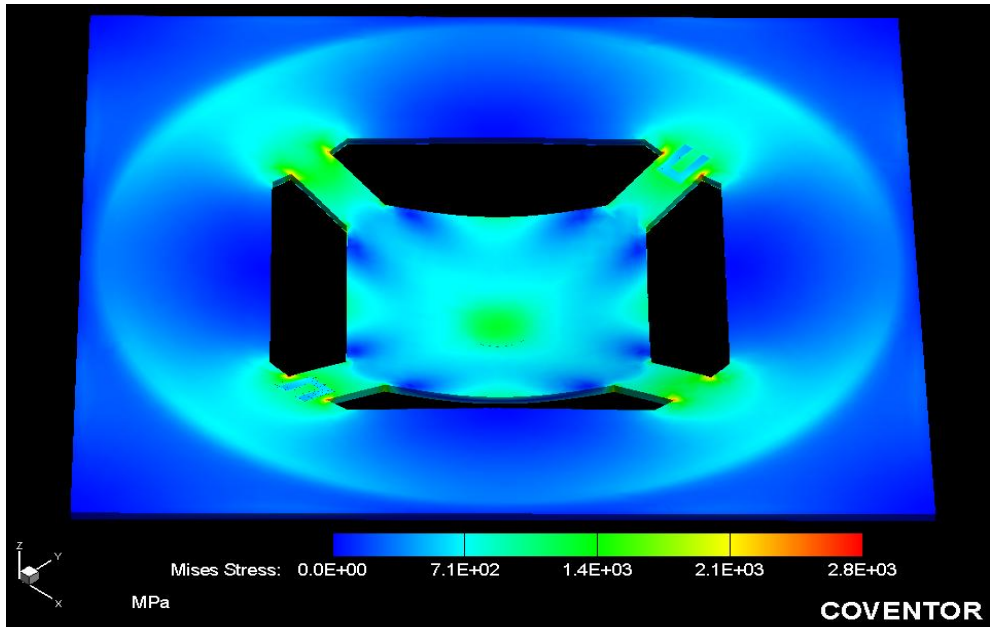


Fig. 2.8 Mises stress for a tactile sensor design T2 without superstrate

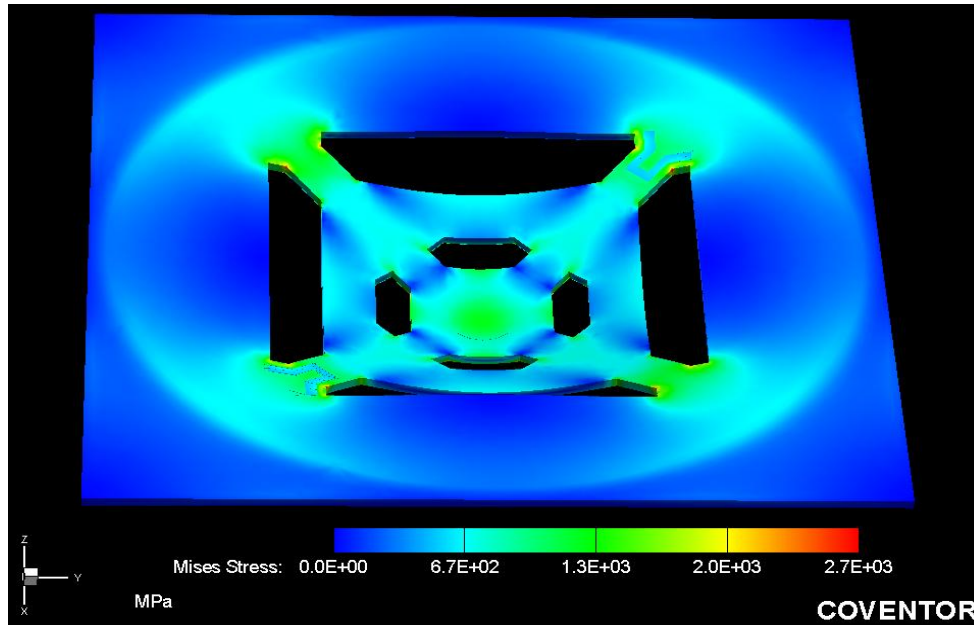



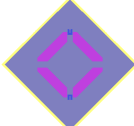

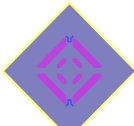
Fig. 2.9 Mises stress for a tactile sensor design T4 without superstrate

The results presented in Table 2.2 are for a membrane thickness of $1.4 \mu\text{m}$ and a sacrificial polyimide thickness of $6.5 \mu\text{m}$. The cavity height or thickness after ashing the sacrificial polyimide layer is crucial for determining the displacement of the membrane in the z-direction. The maximum stress values obtained in Table 2.2 are of aluminium oxide membrane structure and they show that the maximum stress values are far below the material yield strength of 15.4 GPa [47].

2.5 Simulation of Flexible Tactile Sensors with Superstrate

Along with tactile sensor simulation and fabrication, the goal of this thesis is to package the sensors. Choice of materials and their respective thicknesses for the superstrate film were critical factors to be considered. The material used for simulating and packaging the tactile sensors is again polyimide. This protective polyimide layer is called a superstrate.

Table 2.2 Summary of simulated results for flexible tactile sensors

Device notation	Sensor schematic	Shuttle-plate size (μm)	Bridge arm size (μm)	Piezoresistor size (μm)	Piezoresistor shape	Displacement (μm)	Load (MPa)	Maximum Stress (GPa)
T1		80X80	28X14	13.5X2.5	U	5.1	15.5	3.3
T2		80X80	21X14	11.0X2.5	U	5.1	17	2.8
T3		80X80	21X14	9.0X2.5	U	5.1	17	3.6
T4		90X90	14X14	8.0X2.6	Y	5.1	16	2.7

In order to understand the mechanical behavior of the tactile sensors embedded in between the polyimide films: flexible polyimide substrate and superstrate film, simulations have been performed on four different sensor designs. The simulations for tactile sensors with varied thicknesses of the superstrate were checked before choosing the material and the thickness of the film. DuPont™ Kapton® 20EN (nominal thickness: 5.0 μm) and 30EN (nominal thickness: 7.6 μm) were best suited as they are the thinnest flexible polyimide films available. The 20EN superstrate film was used for bonding to the tactile sensor and for simulations. The material properties are shown in Table 2.1. The boundary conditions remain the same for the portion of the structure with the tactile sensor. The four side surfaces of the superstrate are fixed for all degrees of freedom. This can be explained in Fig. 2.11

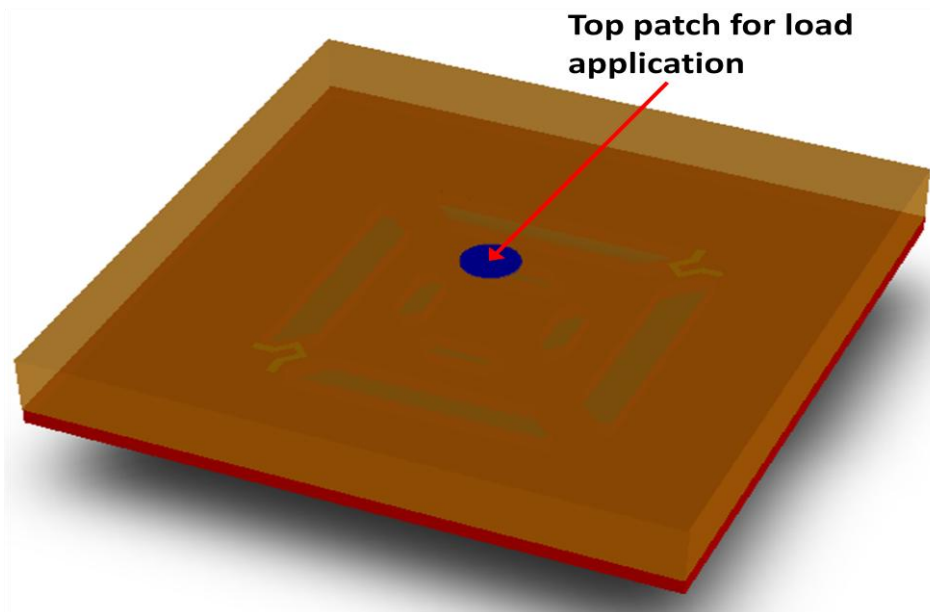


Fig. 2.10 Load application on the 20 μm patch of the superstrate

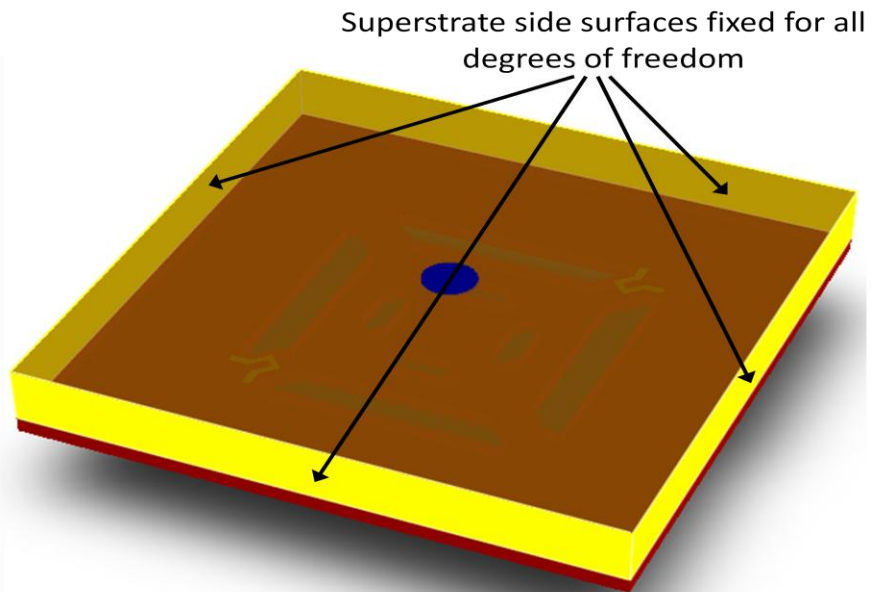


Fig. 2.11 Boundary conditions of the superstrate layer

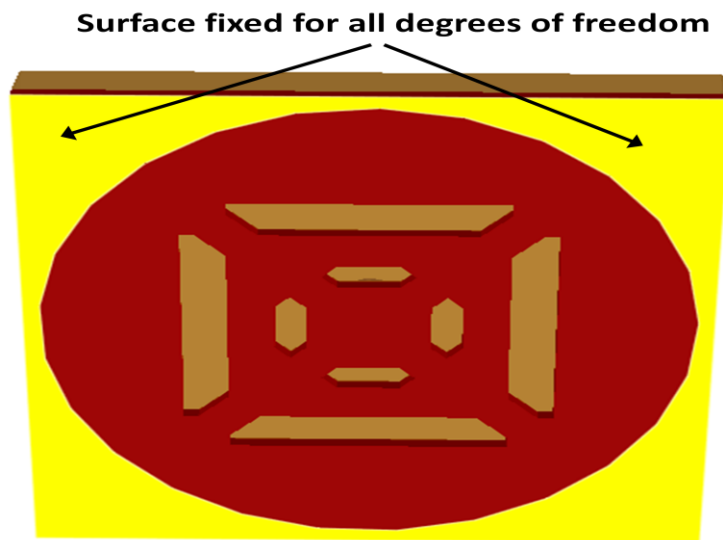


Fig. 2.12 Boundary conditions emulating the ashed sacrificial polyimide layer


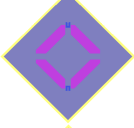
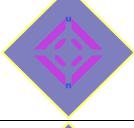
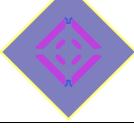
Table 2.3 shows the results for the tactile sensor with superstrate. The thickness of the superstrate, membrane and sacrificial polyimide layer are $5.0\ \mu\text{m}$, $1.4\ \mu\text{m}$ and $6.5\ \mu\text{m}$ respectively.

From the simulations the maximum stress is present in the aluminium oxide membrane and the superstrate acts like a stress absorber. This can be observed for T2 and T4 devices in Figs. 2.13 and 2.14.

2.6 Summary

In this chapter, first an overview is given on the theory of operation of a piezoresistive pressure sensor. Then, an introduction to why a half-Wheatstone bridge configuration is implemented. The procedure used to calculate the gauge factor of the nichrome piezoresistors is explained in detail. The sensor designs and the choice of materials for the MEMS sensor are addressed. The boundary conditions and simulated results have been discussed in detail for tactile sensors with and without a superstrate.

Table 2.3 Summary of simulated results for flexible tactile sensors with superstrate

Device notation	Sensor schematic	Shuttle-plate size (μm)	Bridge arm size (μm)	Piezoresistor size (μm)	Piezoresistor shape	Displacement (μm)	Load (MPa)	Maximum Stress (GPa)
T1		80X80	28X14	13.5X2.5	U	5.1	60	3.0
T2		80X80	21X14	11.0X2.5	U	5.1	61	3.0
T3		80X80	21X14	9.0X2.5	U	5.1	63	4.3
T4		90X90	14X14	8.0X2.6	Y	5.1	58	4.3

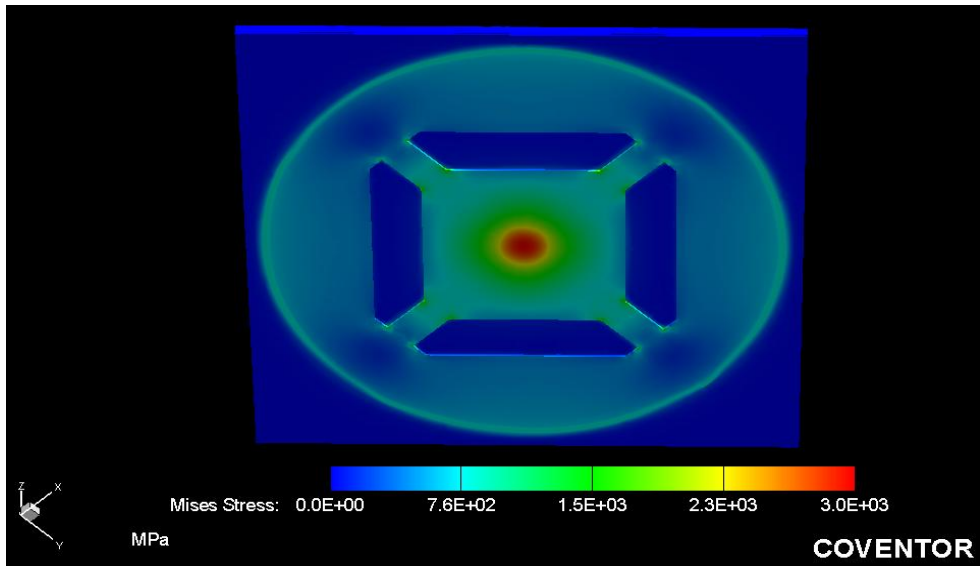


Fig. 2.13 Mises stress for a tactile sensor design T2 with superstrate

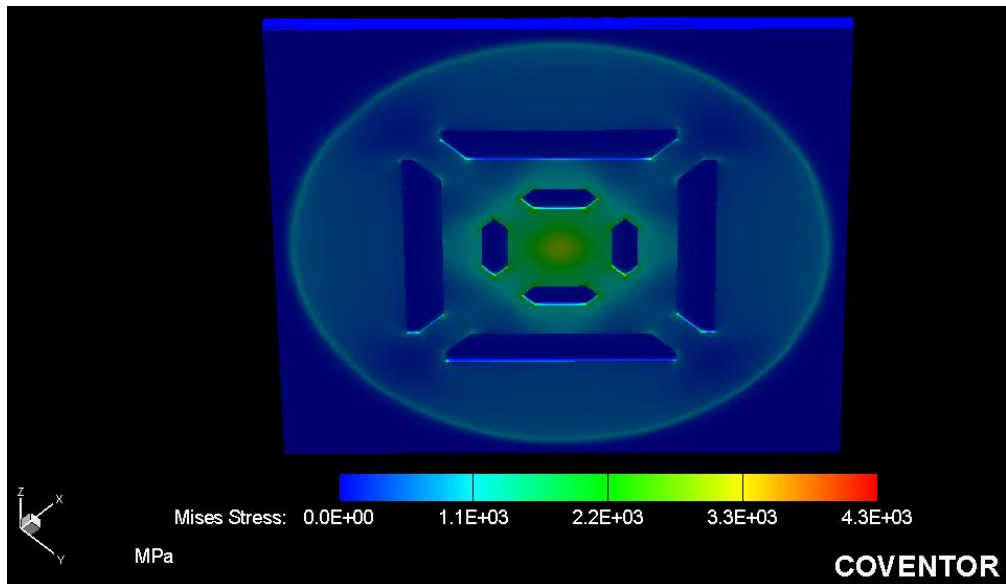


Fig. 2.14 Mises stress for a tactile sensor design T4 with superstrate

CHAPTER 3

FABRICATION

3.1 Fabrication of Flexible Tactile Sensors

MEMS device fabrication processes to a large extent use similar technologies that are used in integrated circuit (IC) fabrication techniques. This Chapter focuses on the fabrication of tactile sensors on flexible substrates. The flexible device is fabricated on a 4 inch Si (100) handle wafer for reasons like: ease in fabrication of multi-layered device structures and alignment of several films when they are to be stacked [16].

The flexible substrate is deposited on top of the silicon handle wafer. Prior to this, wafer cleaning was performed. The degreasing step was done by rinsing the wafer in acetone, methanol, isopropyl alcohol and deionized water baths. After this preliminary step, the wafer was cleaned in acid baths of piranha (3:1 $\text{H}_2\text{SO}_4:\text{H}_2\text{O}_2$) and diluted hydrofluoric acid (HF). The clean wafers are then dehydrated at 100°C for 5 minutes. To remove any presence of contaminants on the surface of the wafer during fabrication, intermediate cleaning steps are incorporated. Prior to each process step, the deposited or patterned layer was cleaned using methanol, isopropyl alcohol and deionized water after which the wafer was dehydrated by baking it at 100 °C for 5 minutes.

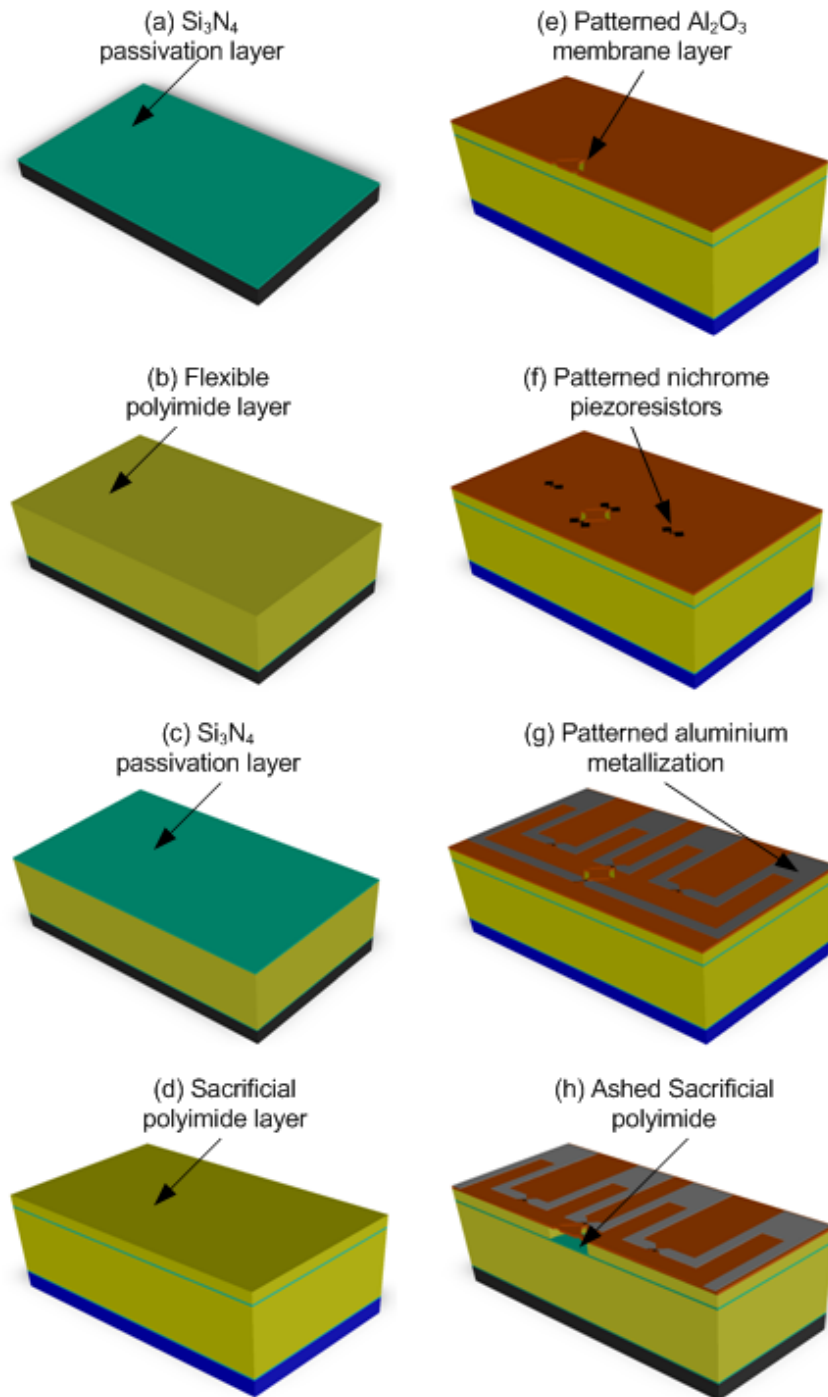


Fig. 3.1 Process flow for the fabrication of a tactile sensor

Fig. 3.1 shows the process flow for the fabrication of the tactile sensor. There are a total of seven layers, all of which were sputter deposited. The Figs. 3.1 (e) to (g) illustrate the layers that were patterned by photolithography and the structure realized by lift-off technique.

The first step in the fabrication process was to sputter deposit silicon nitride (Si_3N_4) on a single-side polished Si (100) wafer. This layer serves as a passivation and planarization layer. A layer thickness of $0.5\ \mu\text{m}$ was deposited over 5 hours using the AJA ATC Orion series sputter system. The required deposition was achieved at the room temperature with gas flow rates of 30 sccm and 5 sccm for Ar and N_2 , respectively. The process pressure was maintained at 2.8 mTorr for an RF power of 150 Watts during the time of deposition. To fabricate the tactile sensors on a flexible layer, next PI 5878 G (HD Microsystems) polyimide was spin-coated at 1500 rpm for 60 seconds followed by a hot plate bake at $110\ ^\circ\text{C}$ for 5 minutes. For the given spin-speed, a film of $6.7\ \mu\text{m}$ thickness was obtained. This step was repeated six times to achieve a total thickness of $40\ \mu\text{m}$. The stacked polyimide is now called flexible polyimide layer. The curing temperature was set to $300\ ^\circ\text{C}$ for 7 hours in a nitrogen gas environment with a ramp up and ramp down rates of $1.5\ ^\circ\text{C}/\text{min}$. After the curing process of the flexible polyimide layer, $0.5\ \mu\text{m}$ of Si_3N_4 passivation was again sputter deposited for 5 hours. The next step includes spin-coating PI 2611 (HD Microsystems) polyimide or called sacrificial polyimide at 4000 rpm for 50 seconds, followed by a hot plate bake at $110\ ^\circ\text{C}$ for 5 minutes. The polyimide is cured at $300\ ^\circ\text{C}$ for 4 hours in nitrogen gas environment with a ramp up and ramp down rates of $1.5\ ^\circ\text{C}/\text{min}$. The final thickness of the cured sacrificial polyimide layer was $6.5\ \mu\text{m}$. The next step included patterning, sputter deposition and lift-off of aluminium oxide (Al_2O_3). This layer serves as the membrane layer. For patterning, a positive photoresist S1813 (Shipley Microposit) was used. As the membrane layer required a lift-off process and as positive photoresists do not have a retrograde slope it makes it difficult for the layer to be lifted off. Therefore, LOR 15B (or Lift-off resist) was utilized. On top of the sacrificial polyimide layer LOR 15B was spin-coated at 2500 rpm for 40 seconds and hot-plate baked at $150\ ^\circ\text{C}$ for 3 minutes. This step was followed by

spin-coating S1813 on the LOR 15B at 2500 rpm for 30 seconds and hot-plate baked at 100 °C for 1 minute. At this stage, the photoresist was exposed under the UV Hg-Arc lamp in the OAI Model 806 i-line contact aligner photolithography unit for 5 seconds for an of exposure energy: 19 mW/cm². After exposure, the photoresist was developed for 3 minutes in MF 319 resist developer.

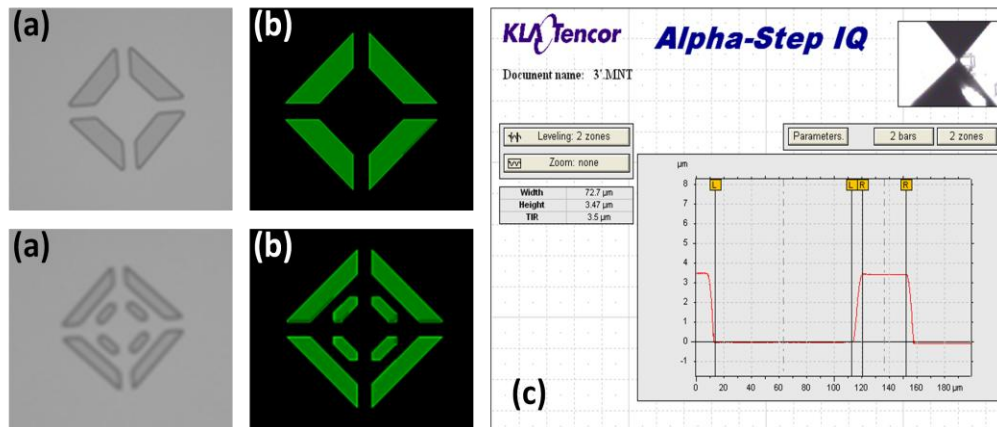


Fig. 3.2 After photolithography using LOR 15B and S1813 (a) Patterned features after photolithography, (b) Mask patterns of the trenches on the diaphragm and (c) Surface profile of the patterned features using S1813 photoresist.

The membrane layer was formed by sputter deposition of Al₂O₃. A layer thickness of 1.2 μm was deposited over 24 hours by sputter-rate studies. The required deposition was achieved at room temperature with gas flow rates of 30 sccm and 5 sccm for Ar and N₂, respectively. The process pressure was maintained at 5 mTorr for an RF power of 150 Watts during the time of deposition. Following Al₂O₃ deposition, the patterned sample was then placed in an acetone and 1165 resist stripper baths (150 ml each) for over a period of two hours for lift-off. The sample was intermittently ultrasonically agitated for 15 minutes at a time during the lift-off period.

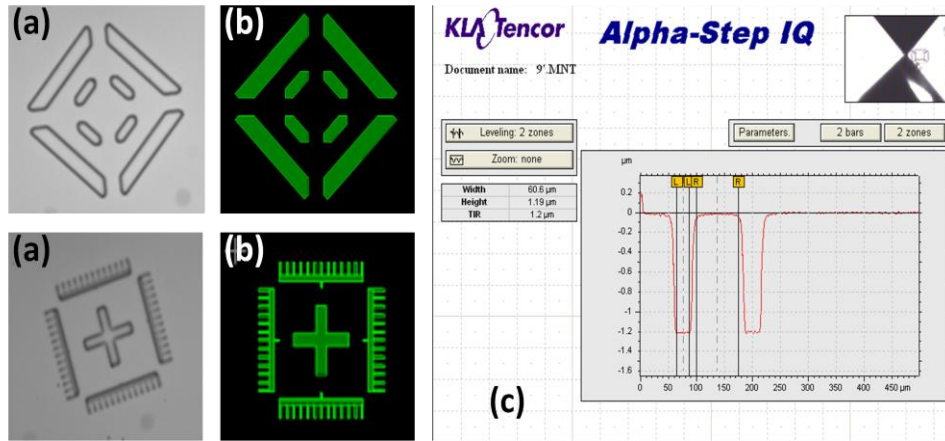


Fig. 3.3 (a) Aluminium oxide membrane layer images, (b) Mask patterns of the trenches on the diaphragm and alignment mark and (c) Surface profile of the aluminium oxide membrane layer.

The piezoresistor deposition was crucial as they are the sensing elements. The piezoresistive material nichrome (NiCr 80/20 wt. %) was patterned by photolithography and realized by lift-off. The alignment of the piezoresistors on the Al_2O_3 membrane was vital and is to be taken care of during the photolithography step. A negative photoresist was used in this case. The photoresist Futurrex NR-9 1500 PY was spin-coated at 2500 rpm for 40 seconds and hot-plate baked at 150 °C for 1 minute. The exposure time was set at 11 seconds during photolithography. The exposed sample was now placed on a hot plate at a post-bake temperature of 100 °C for 1 minute. The sample was developed in RD 6 photoresist developer for 2 minutes 30 seconds. Sputter-rate studies assisted in measuring the thickness of the deposited nichrome film which was 15 nm for 2 minutes. The sputtering was performed at room temperature with a gas flow rate of 50 sccm for Ar gas. The process pressure was maintained at 10 mTorr for an RF power of 60 Watts during the time of deposition. After sputtering the sample was immediately placed in the 1165 resist stripper bath of 150 ml for 30 minutes. As the thickness of the film is only a few hundreds of angstroms it is not advisable to ultrasonically agitate the bath.

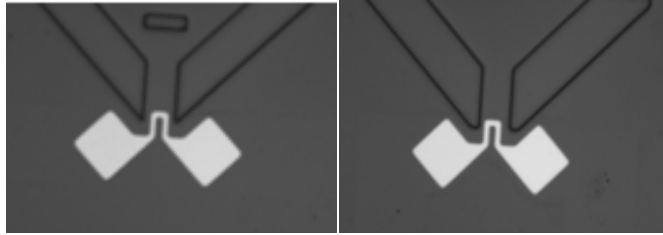


Fig. 3.4 Nichrome piezoresistors after lift-off.

Aluminium (Al) metallization layer was deposited on top of the piezoresistors acting as interconnects to form a half-Wheatstone bridge configuration. The interconnect layer was patterned using negative photoresist NR-9 1500 PY spun-on at 2500 rpm for 40 seconds and hot plate baked at 150 °C for 1 minute. The photoresist was exposed for 11 seconds followed by a post-bake for 100 °C for 1 minute. The development time for the sample was 2 minutes 30 seconds in the RD 6 photoresist developer. Aluminium (Al) was sputter deposited using the AJA ATC Orion UHV series. A thickness of 300 nm Al was deposited in 30 minutes at an RF power of 150 Watts and a process pressure of 2.8 mTorr. The lift-off was performed in an 1165 resist stripper for 30 minutes without any ultrasonic agitation.

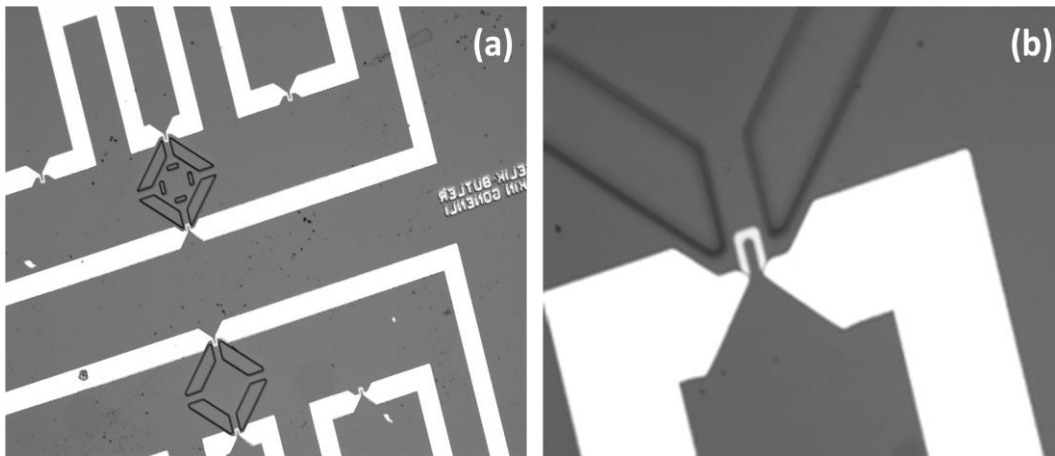


Fig. 3.5 (a) After lift-off of Al metallization and (b) Magnified image of the Al metallization.

The final step involves removing the sacrificial polyimide layer to suspend the tactile sensors. The removal of this sacrificial polyimide was done by ashing, by burning the polyimide in an oxygen rich environment or chamber [4] in the Deiner electronics asher. Upon ashing, the

nichrome piezoresistors had shown a high tendency to oxidize. To prevent oxidation of nichrome, a protective layer of Al_2O_3 was sputter deposited. The protective layer was achieved by performing a photolithography step using NR-9 1500 PY. After patterning, aluminium oxide of thickness $0.18 \mu\text{m}$ was sputtered and lifted off in acetone. With this step, the only exposed regions are the trench regions through which the sacrificial polyimide was ashed and the bond-pad regions are opened to facilitate packaging and testing. The sacrificial polyimide was ashed for around 200 hours (shown in Fig. 3.6). Over ashing the tactile sensors undercut region would change the mechanical characteristics of the device.

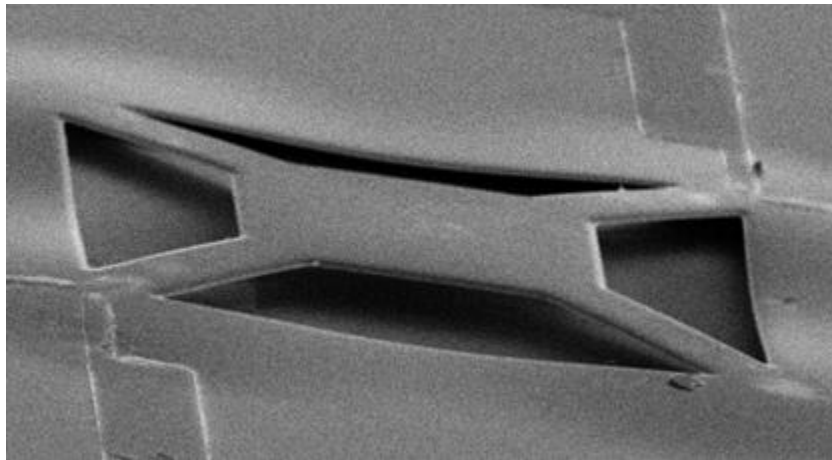


Fig. 3.6 Suspended membrane after ashing the sacrificial polyimide.

3.2 Flexible Tactile Sensor Packaging with a Superstrate

After the flexible tactile sensors were fabricated, packaging was done with a superstrate. The superstrate material should be bonded on to the tactile sensor diaphragm, without hindering its movement. As the sensors were meant to be utilized for prosthetic applications, several commercially available flexible films were readily available for testing. A few of them included: Dragon skin (or injected silicone) [50], silicone [51], silicone rubber [52], Hytrel 8236 [53]. The major problem was to figure out a way to integrate these materials on to the fabricated tactile sensors. DuPont has a series of Kapton polyimide thin film offerings where flexibility, thickness, strength, toughness and wear resistance are clearly documented. Most

importantly these films had been used previously as flexible substrates for varied applications. The Kapton polyimide films 30EN (nominal thickness: 7.6 μm) and 20EN (nominal thickness: 5 μm) were chosen to be the superstrate materials because they had the least thickness compared to the rest of the commercially available flexible films. The choice of the superstrate is vital for better functioning of the tactile sensors. A thick superstrate can decrease the deformation of the membrane at a given applied pressure since the superstrate behaves like a stress absorbent. Therefore, the tactile sensors were bonded to a 20EN film as it has the least thickness among the commercially available flexible films. An adhesive material was used to bond the flexible superstrate to the tactile sensor. The material property of the adhesive is a key factor to be considered for the bonding process to be successful. Most of the commercially available adhesives are 25 μm or 1 mil in thickness. This cannot be integrated on top of the sensor as chances of the adhesive to seep through the trenches of the diaphragm and fill the 6.5 μm thick undercut region were high. The best option available was to use HD Microsystems PI 2555 as the adhesive material. The advantage of utilizing this adhesive polyimide is the lower curing temperature and the thinness of the cured film. The thickness of this layer can be varied between 0.5 μm to 6 μm by setting the spin-speed. An advantage of PI 2555 is that it forms better bonds with oxide and metal surfaces. As the majority of the tactile sensor surface area was made of Al_2O_3 , the bond to the superstrate was not difficult to form.

The first step was wrapping an aluminium foil on to a 4-inch Si wafer. It was of utmost importance that the foil was not wrinkled. The thin Kapton polyimide 20EN film was placed on top of the foil. As the superstrate film was very thin, it conformed to the surface of the foil. At this stage, the adhesive PI 2555 was dispensed on the superstrate film. The film along with the adhesive was then spin-coated at 5000 rpm for 30 seconds to achieve a thickness of 1.5 μm . Then, the tactile sensors active surface had to be placed facing the adhesive. At this step the stacked layers of tactile sensor die, adhesive and superstrate film were to be heat-treated upon a hot-plate. The sample was heat-treated from 120 $^{\circ}\text{C}$ to 150 $^{\circ}\text{C}$ at increments of 10 $^{\circ}\text{C}$ for

every 5 minutes before curing. This stack was subsequently placed in a Blue M inert atmosphere oven and cured at 200 °C for 1 hour. Fig. 3.8 shows the bonded structure of the tactile sensor to the superstrate.



Fig. 3.7 (a) Adhesive polyimide being dispensed on the superstrate and (b) Tactile sensor die placed on the superstrate for heat treatment.

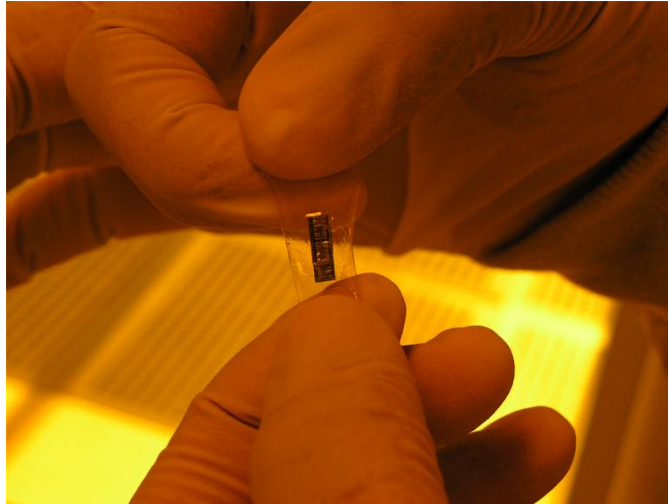


Fig. 3.8 Superstrate bonded to the tactile sensor die.

After bonding the superstrate to the tactile sensor die, it was imperative to open the bond-pad regions in order to attain electrical connectivity. The bond-pads on the mask (Fig. A.5) were aligned to the ones on the tactile sensor die. Positive photoresist S1813 was used to pattern the bond-pads. The photoresist was spin-coated at 2000 rpm for 30 seconds followed by

a pre-bake of 115 °C for 1 minute. The photoresist was then exposed for 6 seconds at an exposure energy of 19.6 mW/cm² and developed in MF 319 for 2minute 30 seconds. Aluminium oxide was sputter deposited for 3 hours to achieve a thickness of 0.18 µm, after which lift-off was performed in acetone. The deposited film acts as a hard mask when the superstrate was being etched. The etching was performed using the deep reactive ion etcher (DRIE) of the TRION series. The polyimide was etched in 8 minutes opening up the Al bond-pads for electrical connectivity. The gases used were O₂ (70 sccm) and CF₄ (30 sccm). The chamber pressure was maintained at 100 mTorr for an RIE (reactive ion etching) power of 100 Watts and ICP (inductively coupled plasma) power of 3000 Watts. Fig. 3.9 (c) shows the profile of the etched superstrate.

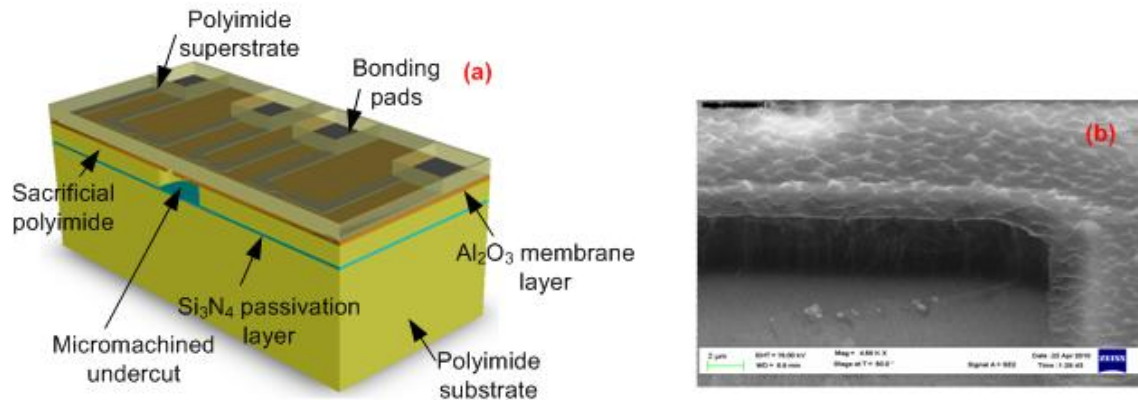


Fig. 3.9 Solid model of the superstrate bonded to the tactile sensor (a) 3D model of the tactile sensor with superstrate and (b) Close-up onto the edge of the bonding pads.

3.3 Summary

This Chapter details the fabrication of a flexible tactile sensor and bonding to a superstrate film. Different fabrication steps were implemented and their importance has been addressed. Explanation is given as to why a particular kind of superstrate material and adhesive material had been selected.

CHAPTER 4

ELECTRICAL CHARACTERIZATION

In this Chapter the electrical characterization results for flexible tactile sensors without and with a superstrate are presented.

4.1 Flexible Tactile Sensor Characterization without and with a Superstrate

4.1.1 I-V Measurements

Electrical characterization of the tactile sensor with and without a superstrate has been performed using a semiconductor parameter analyzer Agilent 4155C. In order to measure the current-voltage (or $I-V$) characteristics the parameter analyzer was connected to a probe-station. The probe-tips of the micro-manipulators on the station were utilized to probe or electrically connect to the bond-pads of the tactile sensor. The $I-V$ characteristics were used to measure the pseudo resistance values of A_1, A_2, P_1, P_2 . All four piezoresistors are placed in a half-Wheatstone bridge configuration (Fig. 2.2). They are termed pseudo resistance values because each individual piezoresistor is in parallel to the other three piezoresistors during the measurements. For example, when the piezoresistive value for A_1 is being measured it is the equivalent resistance of A_1 in parallel with $P_1 + A_2 + P_2$ piezoresistors (Fig. 4.1).

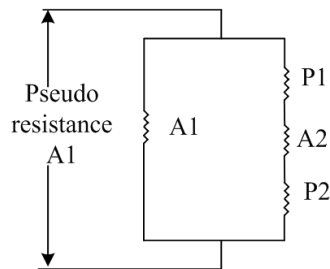
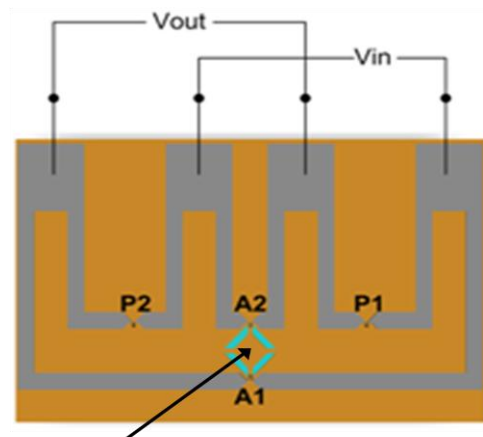


Fig. 4.1 Pseudo resistance of A_1

Once the pseudo resistances are obtained using the slope of the $I-V$ curve, the actual individual resistances are computed using the MATLAB™ code in APPENDIX B.2. The same procedure was performed to measure and acquire the individual resistances of the piezoresistors for the tactile sensors without and with the superstrate. The results are consolidated in Tables 4.1 and 4.2. The $I-V$ plots for these sensors are shown in APPENDIX C.1.

4.1.2 Response Measurements

To calculate the tactile sensor output, response measurements were performed. Fig. 4.2 represents the setup to determine the sensor output response. At first, offset voltage was measured without any application of load on the membrane. This voltage was determined for four different configurations by interchanging the input (V_{in}) and output (V_{out}) ports as well as changing the input bias polarity. The configuration giving the least value of the offset voltage was used for response measurements. The experimentally acquired offset voltage was theoretically verified with the MATLAB™ program in APPENDIX B.2. The input bias voltage was applied to the input ports (V_{in}) and the output was measured across the output ports (V_{out}).



Probe to apply pressure on the membrane

Fig. 4.2 Illustration of the setup to measure the tactile sensor output

Table 4.1 Results for tactile sensors without superstrate



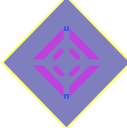
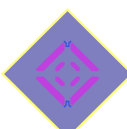

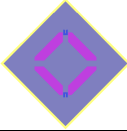


Device notation	Sensor schematic	Shuttle-plate size (μm)	Bridge arm size (μm)	Piezoresistor size (μm)	Piezoresistor shape	Displacement (μm)	Load (MPa)	Device #	Individual Resistances (Ohms)				$\Delta R/R$	Gauge Factor
									A1	A2	P1	P2		
T1		80X80	28X14	13.5X2.5	U	5.1	15.5	I	7840	8510	8810	8530	6.20e-2	1.50
								II	7340	7750	7770	8170	5.61e-2	1.36
T2		80X80	21X14	11.0X2.5	U	5.1	17	I	8840	9330	9090	9560	2.79e-2	1.06
								II	7820	8160	8290	8370	4.34e-2	1.64
T3		80X80	21X14	9.0X2.5	U	5.1	17	I	5100	5480	5800	5660	8.39e-2	5.77
T4		90X90	14X14	8.0X2.6	Y	5.1	16	I	7280	9760	8030	7880	5.60e-2	2.70
								II	6760	7180	7370	7470	6.63e-2	3.20

Table 4.2 Results for tactile sensors with superstrate

Device notation	Sensor schematic	Shuttle-plate size (μm)	Bridge arm size (μm)	Piezoresistor size (μm)	Piezoresistor shape	Displacement (μm)	Load (MPa)	Device #	Individual Resistances (Ohms)				$\Delta R/R$	Gauge Factor
									A1	A2	P1	P2		
T1		80X80	28X14	13.5X2.5	U	5.1	60	I	77 80	65 80	66 20	73 60	2.59 e-2	0.91 9
								II	87 50	78 50	88 90	90 10	8.05 e-2	2.85
T2		80X80	21X14	11.0X2.5	U	5.1	61	I	78 30	81 70	82 90	83 70	4.07 e-2	2.20
T3		80X80	21X14	9.0X2.5	U	5.1	63	I	63 00	57 70	55 80	55 80	7.33 e-2	7.02
								II	50 50	47 80	46 70	45 70	6.07 e-2	5.81
T4		90X90	14X14	8.0X2.6	Y	5.1	58	I	67 70	71 80	73 70	74 70	6.28 e-2	7.87

The bias voltage at V_{in} was varied from 0.5 to 2.0 Volts using the semiconductor parameter analyzer 4155C. The voltage value obtained across the output ports is called the offset voltage. In order to determine the response of the device when load is applied, the membrane was deflected with a probe-tip of diameter 20 μm . The membrane is deflected completely for a displacement of 5.1 μm until it touches the bottom of the cavity. While the load is applied, the bias voltage is swept again across the input ports to determine the final output voltage. The difference in the final output voltage and the offset voltage provides the change in voltage or differential output voltage (ΔV). The V_{input} vs ΔV measurements were repeated at least six times. The average value of the slopes of all plots for a device was fed in to the MATLAB™ code to acquire $\Delta R/R$.

4.1.2.1 Response Measurement Results for Tactile Sensors without a Superstrate

Table 4.3 shows the offset and differential voltages for tactile sensors without a superstrate. The offset voltage was measured at 1 V input bias voltage for all devices. The range of the offset voltage was between 13.3 mV for T2 device to 39.8 mV for T3 device type. The maximum differential voltage of 0.80 mV is seen for device T4. The results for the normalized change in resistance for these devices are given in Table 4.1. The response measurements for these devices are plotted in Figs. 4.3 to 4.6.

4.1.2.2 Response Measurement Results for Tactile Sensors with a Superstrate

The offset and differential voltage results for tactile sensors with a superstrate are presented in Table 4.4. The range of the offset voltage is between 12.8 mV for T1 device to 38.6 mV for T3 device. The maximum change in voltage of 0.74 mV is seen for device T4. The results for the normalized change in resistance for these devices are given in Table 4.2. The response measurements for these devices are plotted in Figs. 4.7 to 4.10.

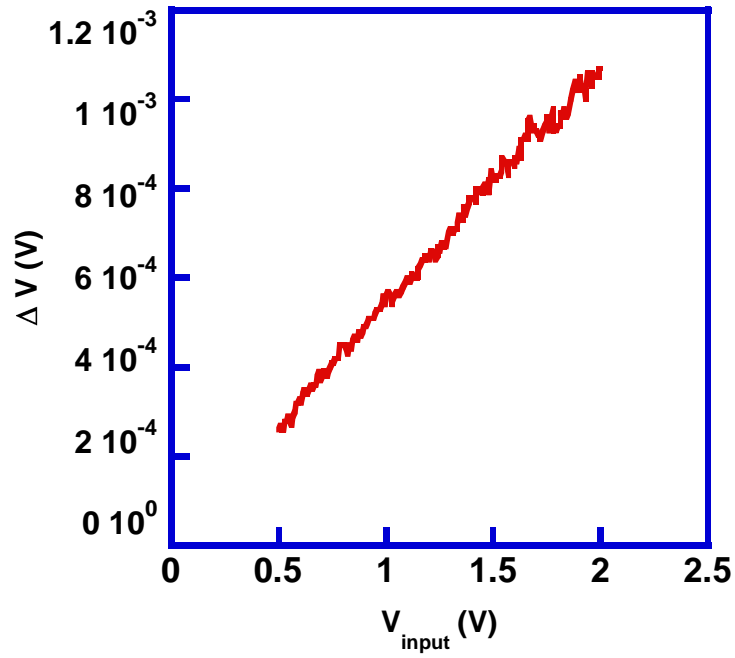


Fig. 4.3 Change in output voltage with load vs Wheatstone bridge input voltage for T1 device # 1 without a superstrate

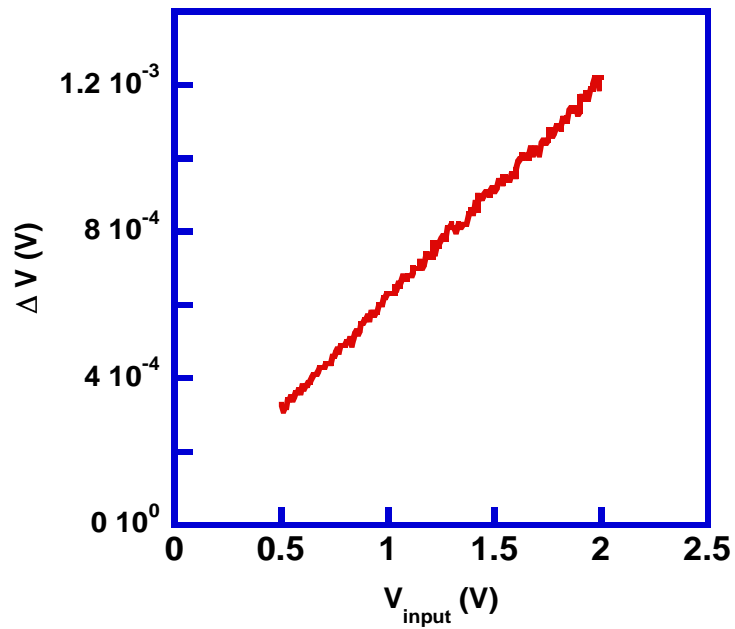


Fig. 4.4 Change in output voltage with load vs Wheatstone bridge input voltage for T2 device # 1 without a superstrate

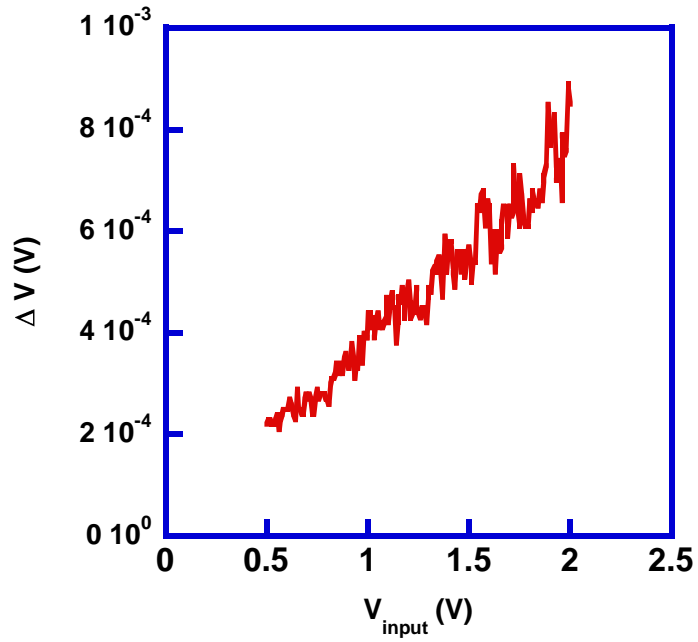


Fig. 4.5 Change in output voltage with load vs Wheatstone bridge input voltage for T3 device # I without a superstrate

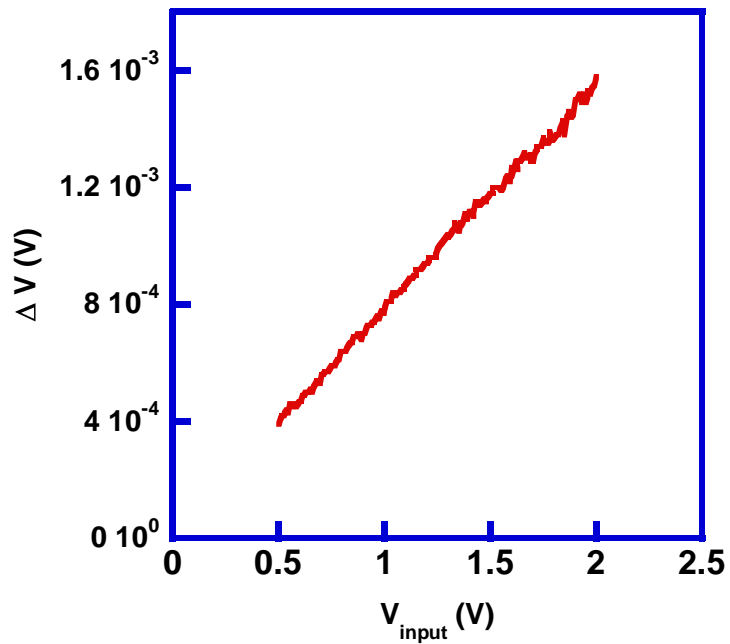


Fig. 4.6 Change in output voltage with load vs Wheatstone bridge input voltage for T4 device # II without a superstrate

Table 4.3 Offset voltage and differential voltage results for devices without a superstrate for 1V input bias voltage

Device notation	Load (MPa)	Displacement (μm)	Device #	Offset voltage (mV)	Differential voltage, ΔV (mV) *
T1	15.5	5.1	I	29.3	0.56
			II	27.1	0.32
T2	17	5.1	I	13.3	0.62
			II	20.4	0.54
T3	17	5.1	I	39.8	0.44
T4	16	5.1	I	28.7	0.57
			II	31.2	0.80

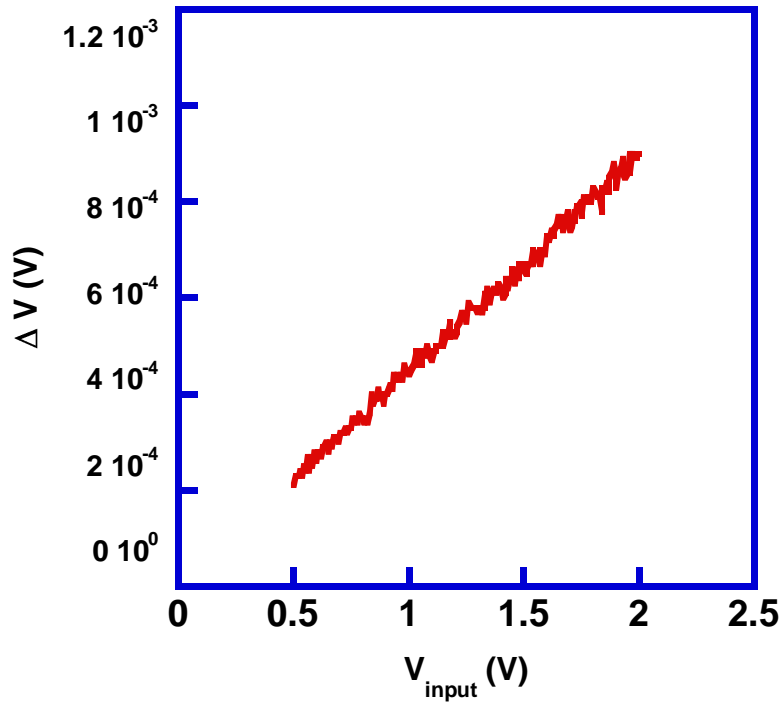


Fig. 4.7 Change in output voltage with load vs Wheatstone bridge input voltage for T1 device # II with a superstrate

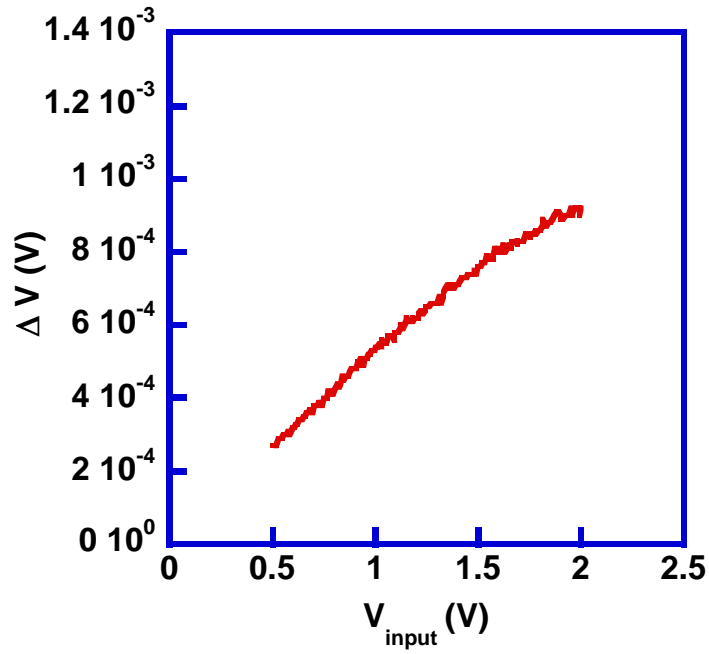


Fig. 4.8 Change in output voltage with load vs Wheatstone bridge input voltage for T2 device # 1 with a superstrate

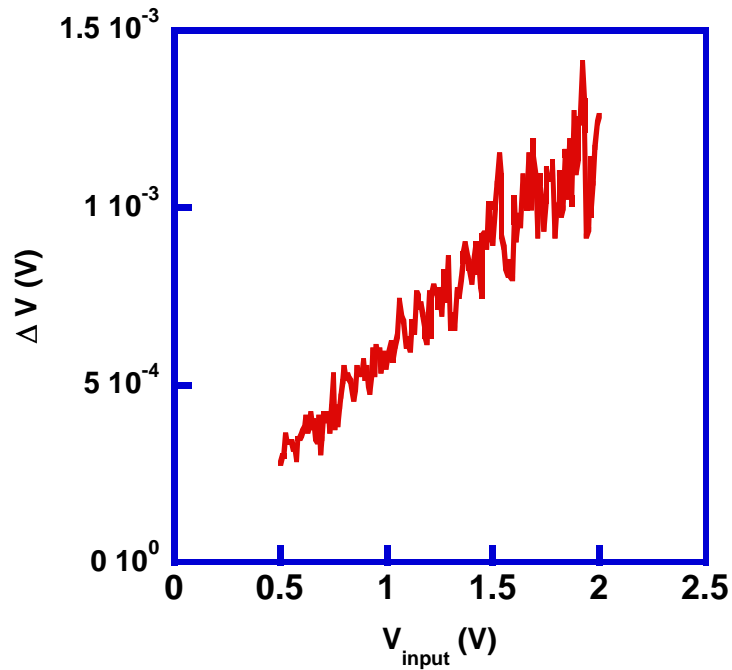


Fig. 4.9 Change in output voltage with load vs Wheatstone bridge input voltage for T3 device # 1 with a superstrate

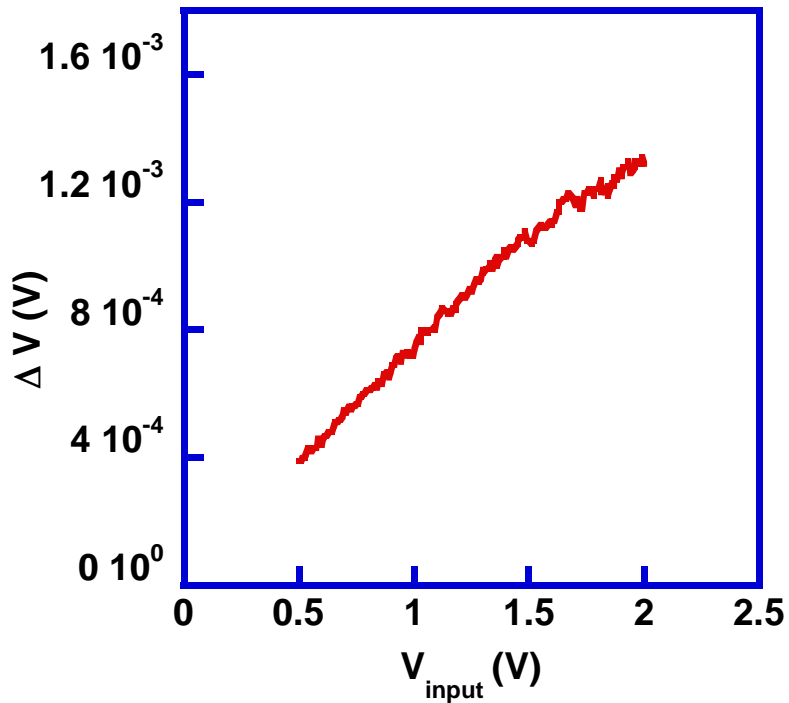


Fig. 4.10 Change in output voltage with load vs Wheatstone bridge input voltage for T4 device # I with a superstrate

Table 4.4 Offset voltage and differential voltage results for devices with a superstrate for 1V input bias voltage

Device notation	Load (MPa)	Displacement (μm)	Device #	Offset voltage (mV)	Differential voltage, ΔV (mV) *
T1	60	5.1	I	12.8	0.52
			II	38.5	0.48
T2	61	5.1	I	20.3	0.54
T3	63	5.1	I	38.6	0.57
			II	31.3	0.52
T4	58	5.1	I	30.2	0.74

The value for the load cannot be determined using the probe-station setup as the micro-manipulators are not equipped for this application. The load or pressure that has been applied to the tactile sensors was computed by simulating in Coventorware™ for a displacement of 5.1

μm with a probe-tip diameter of $20\ \mu\text{m}$. The simulations were repeated for sensor with and without a superstrate.

4.1.3 Gauge Factor Measurements

Gauge factor was calculated with the help of both the response measurements and the simulation results for the tactile sensor without and with a superstrate. As explained in the Sections 2.4 and 2.5, all simulations for the devices were performed for full displacement of the membrane. In the simulations, the probe-tip is represented by a patch of diameter $20\ \mu\text{m}$. Procedure to extract and calculate the average strain is detailed in Section 2.2. Fig. 4.11 shows the Mises stress for device types T2 and T4. Experimentally obtained response measurements are utilized to calculate the normalized change in resistance ($\Delta R/R$) with the help of differential output voltage (ΔV). Finally, by substituting the values of average strain and $\Delta R/R$ in Eq. 2.5 the gauge factor of nichrome is found. The gauge factor results for all characterized devices are shown in Tables 4.1 and 4.2.

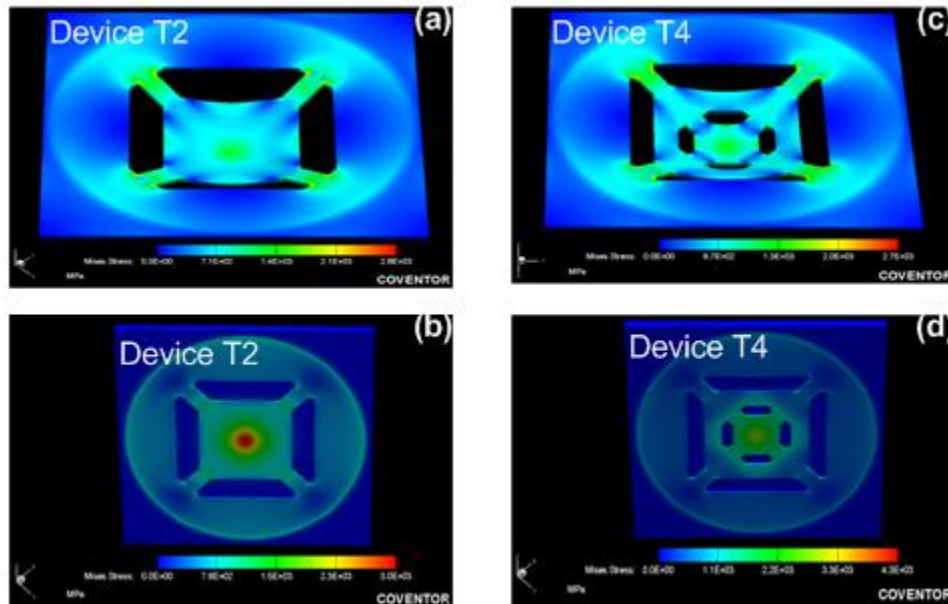


Fig. 4.11 (a), (c) Mises stress simulations for device types T2 and T4 without superstrate and (b), (d) Mises stress for device types T2 and T4 with superstrate

4.2 Discussion

Four different tactile sensor designs: T1, T2, T3, and T4 (Table A.1) were simulated and characterized for the cases without and with a superstrate. Maximum stress, average strain and displacement of the membrane were obtained by extracting the stress values from CoventorWare[®]. With the application of pressure, change in voltage (ΔV) and normalized change in resistance ($\Delta R/R$) were calculated. For tactile sensors without a superstrate the gauge factor values ranged from 1.50 for device T1 to 5.77 for device T3. The gauge factors for tactile sensors with a superstrate ranged between 2.20 for device type T2 to 7.87 for device T4. Applied pressure varies between 15 MPa to 17 MPa on the tactile sensors without superstrate resulting in maximum stress of 2.7 GPa to 3.3 GPa. The pressure ranges being on the higher side, it can be concluded that the membrane undergoes a large deflection. Due to the existence of the superstrate, higher pressure is required to obtain the same membrane deflection as the device without the superstrate. The values of applied pressure range between 58 MPa to 63 MPa for the devices with superstrate with the maximum stress ranging between 3.0 GPa to 4.3 GPa. The superstrate behaves like a stress absorber and thus enables the tactile sensor to withstand high applied pressures. The characterization of the tactile sensors with the superstrate presented another advantage which is protection of the membranes from physical damage.

Process variations in the piezoresistor dimensions, contact resistance and metal interconnects are the cause for the presence of offset voltage in the half-Wheatstone bridge. Although the offset voltage values for the tactile sensors are on the lower side (10 mV to 40 mV) they are present due to the dissimilar individual resistances comprising the bridge. The percent normalized change in resistance for the tactile sensors without superstrate range between 2.79% to a maximum of 8.39%. The $\Delta R/R\%$ for sensors with the superstrate bonded range from 2.59% to 8.05%.

The plots in Figs. 4.2 to 4.5 show the V_{input} vs ΔV for tactile sensors without a superstrate. The plots for device types T1, T2 and T4 have a linear curve showing a consistent change in voltage for increase in the input voltage from 0.5 to 2.0 V. The same trend was seen for tactile sensors with a superstrate when T1, T2 and T4 were characterized (Figs. 4.6, 4.7 and 4.9). The plot for device type T3 was linear with very little fluctuations for both with and without a superstrate cases for an input voltage of 0.5 to 1.0 V. From 1.0 to 2.0 V there was an increasing trend in the fluctuations (Figs. 4.4 and 4.8). Consistent values of offset voltage and output voltage were seen when the input voltage was fixed at discrete values (for example: 0.5 V, 1 V, 1.5 V, 2 V) instead of sweeping it from 0.5 to 2.0 V. The fluctuations in the plots most likely are due to poor probe contact and electrical noise. The maximum calculated gauge factor values are 5.77 and 7.02 for device T3 for without and with a superstrate. The device types T3 and T4 have windows on the membrane but only device T4 sustained the cyclic loading compared to the former. T3 devices were seen to break after a few loading and unloading cycles. Device T4 has better values of normalized change in resistance, differential voltage and gauge factor values. This could be attributed to its slightly bigger shuttle-plate size, smaller piezoresistor size compared to T1, T2 and T3, bridge arm size and Y-shaped piezoresistor.

4.3 Summary

In this chapter, the electrical characterization results for tactile sensors are presented for sensors with and without a superstrate. The procedure by which current-voltage measurements have been performed to determine the piezoresistance values has been explained. Method by which the response measurements have been experimentally performed has been addressed. The results and procedure used to calculate the gauge factor of the nichrome piezoresistors are presented.

CHAPTER 5

CONCLUSION

Microelectromechanical flexible tactile sensors have been simulated, fabricated and characterized. The tactile sensors were fabricated on a flexible polymer substrate and at a later stage were bonded to a flexible polymer superstrate. All the surface micromachining process steps performed in order to fabricate the device are IC compatible. The electrical characterization results of the tactile sensors without and with a superstrate have been presented. The simulation results were verified against the experimentally obtained results and were found to be comparable. The values of the applied pressure were obtained from the simulation results. The simulation 3-D models were made sure to replicate the dimensions of the fabricated devices for proper acquisition of data: maximum stress, displacement magnitude, average strain.

The major goal of this research was to bond a flexible polymer superstrate to the flexible tactile sensor die. A novel process by which the superstrate is mounted and fixated to the top of the tactile sensor has been presented. From the characterization and simulation results the mechanical behavior of the superstrate has been determined. The superstrate film plays a dominant role as it is bonded to a corrugated membrane or diaphragm thus impeding the displacement of the membrane. In order to perform the response measurements for a full deflection of the membrane layer in the cavity, greater range of pressure had to be applied because of the presence of the superstrate. Although the applied pressure is very great the flexible polymer superstrate behaves like a stress absorber and protects the tactile sensor from failing under such high pressures.

The gauge factor results of nichrome piezoresistors on tactile sensors without and with the superstrate are comparable to each other.

APPENDIX A

FLEXIBLE TACTILE SENSOR DESIGNS

A.1 Introduction

Ten pressure sensor structures were designed by Gonenli et al. and utilized for this thesis [43]. The sensors were designed with variations in membrane sizes, bridge arm lengths, shape and length of the piezoresistors (U and Y shaped). Simulations were performed by applying a pressure on the surface of a patch (diameter: 20 μm). Membrane displacement and maximum stress values were directly obtained from the simulation results.

In this section, the two-dimensional layout of the mask patterns and the sensor dimensions are shown.

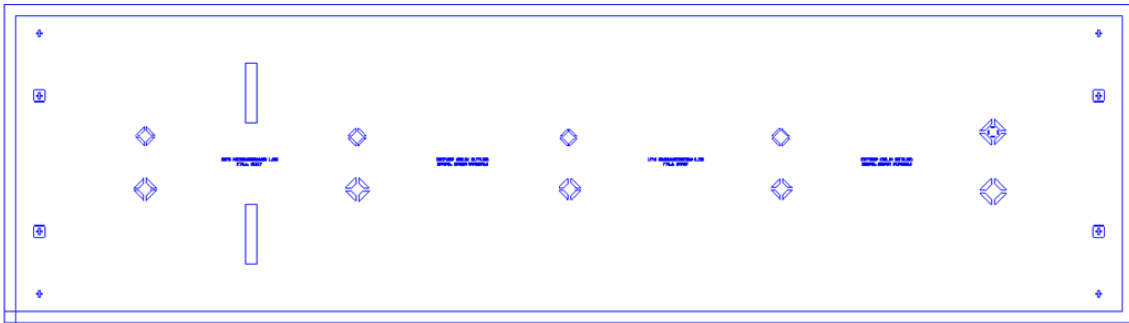


Fig. A.1 Trench mask layout

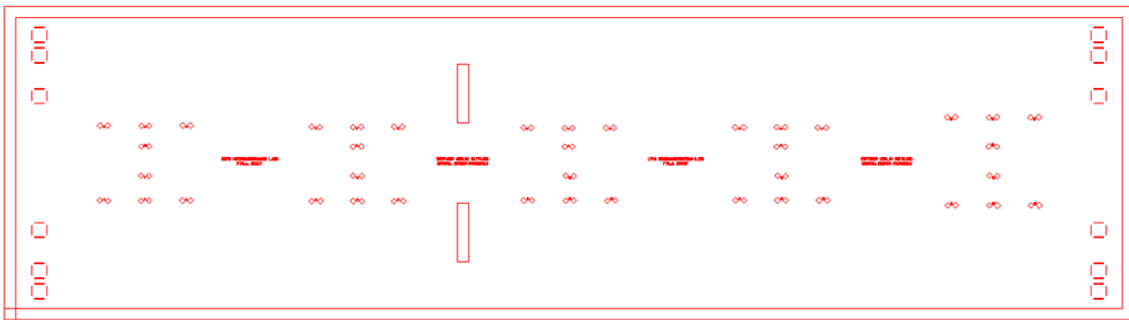


Fig. A.2 Piezoresistor mask layout

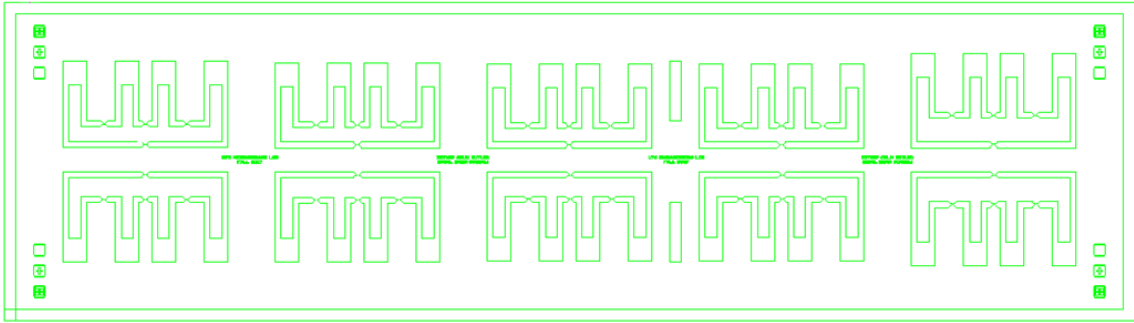


Fig. A.3 Metallization mask layout

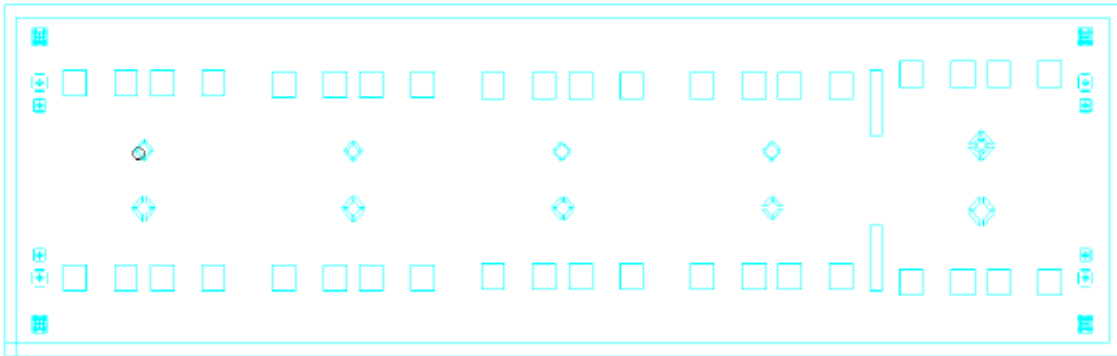


Fig. A.4 Passivation mask layout

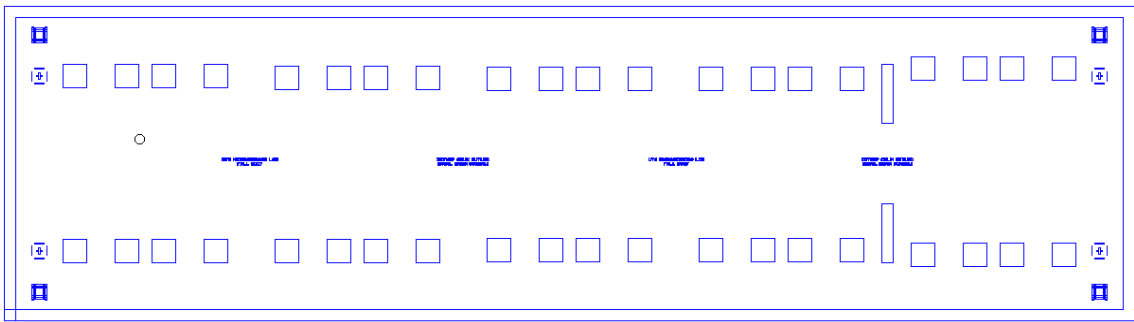

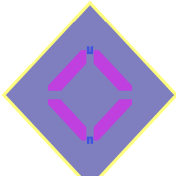
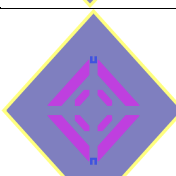
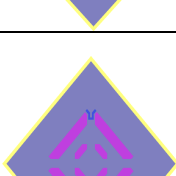


Fig. A.5 Bond-pad mask layout

Four different devices were chosen as their explanation will be given in detail in the chapter where the results will be discussed. Table A.1 gives the dimensions of the devices used in the simulations.

Table A.1 Different pressure sensor designs

Device notation	Sensor schematic	Shuttle-plate size (μm)	Bridge arm size (μm)	Piezoresistor size (μm)	Piezoresistor shape
T1		80X80	28X14	13.5X2.5	U
T2		80X80	21X14	11.0X2.5	U
T3		80X80	21X14	9.0X2.5	U
T4		90X90	14X14	8.0X2.6	Y

APPENDIX B

FLEXIBLE TACTILE SENSOR SIMULATION SETTINGS AND CALCULATIONS

B.1 Introduction

In this section, tactile sensor simulations for devices with and without the superstrate are illustrated. MATLAB™ code used for $\Delta R/R$ and average strain calculations are provided. Simulation settings are given in detail.

B.2 MATLAB™ code for calculating $\Delta R/R\%$

```
clc
Pseudo_P1=6896;
Pseudo_A1=6752;
Pseudo_P2=7128;
Pseudo_A2=7006;
P1=100;
A1=50;
P2=100;
A2=20;
for i=1:10000000
    A_P1=1/((1/Pseudo_P1)-1/(A1+P2+A2));
    A_A1=1/((1/Pseudo_A1)-1/(P1+P2+A2));
    A_P2=1/((1/Pseudo_P2)-1/(A1+P1+A2));
    A_A2=1/((1/Pseudo_A2)-1/(P1+P2+A1));
    P1=A_P1;
    A1=A_A1;
    P2=A_P2;
    A2=A_A2;
end
P1
A1
P2
A2
V_before=.01420;
V_after=.01369;
V_bias=1;
%delV=V_after-V_before;
%V_sum=V_before+delV
p=V_after/V_bias;
a=(p+1);
b=p*(P1+P2+A1+A2)+A1+A2;
c=p*(P1+A1)*(P2+A2)-(P1*P2)+(A1*A2);
root_delR1=(-b+sqrt(b^2-4*a*c))/(2*a)
root_delR2=(-b-sqrt(b^2-4*a*c))/(2*a)
%calculating root delR1:
%Assuming the change in resistance in the active resistors is the same:
%If the average of Active resistors delR1 are taken into consideration for:
R_average=(A1+A2)/2;
percentage_of_delR1byR_alt=(root_delR1/R_average)*100
%calculating root delR2:
```

%If the average of Active resistors delR2 are taken into consideration for:

```

R_average=(A1+A2)/2;
percentage_of_delR2byR_alt=(root_delR2/R_average)*100
V_before
x=((P1*P2)-(A1*A2));
y=((P1+A1)*(P2+A2));
V_offset_1=(x/y)*V_bias
w=((A2*A1)-(P1*P2));
z=((A2+P2)*(P1+A1));
Percentage_decrease_1=((V_before-V_offset_1)/V_before)*100
Percentage_increase_1=((V_offset_1-V_before)/V_offset_1)*100
V_offset_2=(w/z)*V_bias
Percentage_decrease_2=((V_before-V_offset_2)/V_before)*100
Percentage_increase_2=((V_offset_2-V_before)/V_offset_2)*100

```

B.2 MATLAB™ code for calculating average strain

Simulation results were used to find the strain values of ϵ_{xx} and ϵ_{yy} . The images of U-shaped and Y-shaped piezoresistors are given in Fig. B.1. After simulating, the average strain can be calculated from splitting the piezoresistor's area into regions.

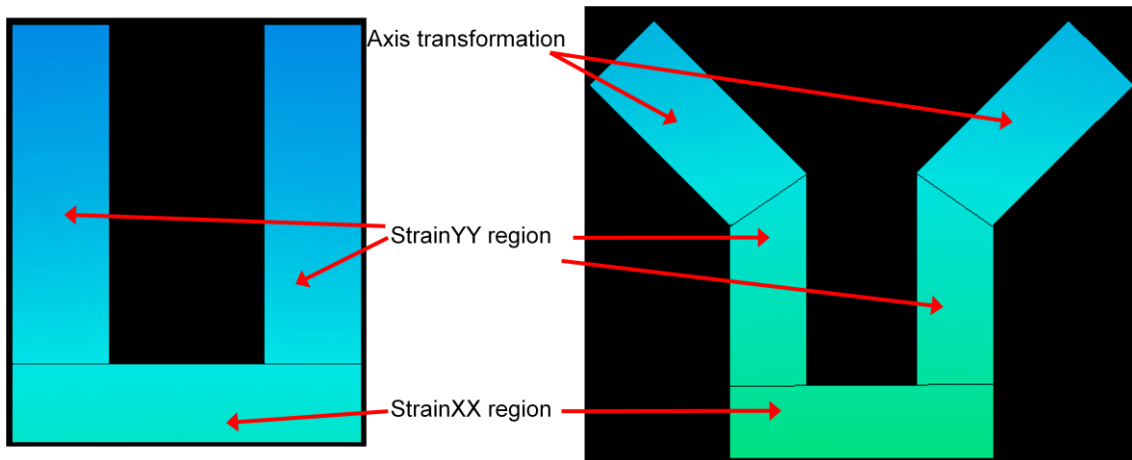


Fig. B.1 Description of U and Y shaped piezoresistors

Axis transformation is explained in Chapter 1. Matlab™ code was used to extract the excel file data to give total strain and total area of a particular region. In turn, this is used to calculate the average strain by using Eq. 2.5.

```

% reads an excel file and extracts useful data to plot
% also reads the data headers that precede the data

```

```

%reading the xls file (in the same directory)
[raw_data,header_info] = xlsread('big_ui_longitudinal.xls')

%data in the xls file is arranged as
% Col 3, Col 4, Col 2
% X      Y      strain
X=raw_data(:,3); %column 1
Y=raw_data(:,4); % column 2
strain=raw_data(:,2); % column 3

mydata = [X Y strain];

minX=min(X); minY=min(Y);
maxX=max(X); maxY=max(Y);
% Define the grid density
m=250;% No. of rows
n=250;% No. of columns

% Make a X x Y grid, called [Xi,Yi]
x1 = linspace(minX,maxX,n);
y1 = linspace(minY,maxY,m);
[Xi,Yi] = meshgrid(x1,y1);

%map mag on to the grid
straini=griddata(X,Y,strain,Xi,Yi);

%generate the mesh plot or just the contours
%[C,h]=contour(y1,z1,magi), title('Device 1b4 Area Scan 8'),...
mesh(x1,y1,straini), title('Plot of strain_y as a function of X and Y'),...
xlabel('x (microns)'),ylabel('y (microns)'),zlabel('Strain_Y');
%set(axes_handle,'YGrid','on')
%clabel(C,h);
view([-37.5,30]);

minstr = min(min(straini));
maxstr = max(max(straini));
AvgStr = 0;
TotalArea = 0;
for i = 1:249
    for j = 1:249
        if mean(straini(i:i+1, j:j+1)) >= minstr & mean(straini(i:i+1, j:j+1)) <= maxstr
            AvgStr = AvgStr + mean(straini(i:i+1, j:j+1)) * (Xi(i, j+1) - Xi(i, j)) * (Yi(i+1, j) - Yi(i, j));
            TotalArea = TotalArea + (Xi(i, j+1) - Xi(i, j)) * (Yi(i+1, j) - Yi(i, j));
        end
    end
end
TotalArea
AvgStr

```

B.3 Simulation Settings

First layout files with the dimensions are drawn using the CAD tool on CoventorWare™. This file represents a two-dimensional layout which is later extruded using the process file to form a three dimensional structure. The Fig. B.2 shows the layout file for a tactile sensor without superstrate.

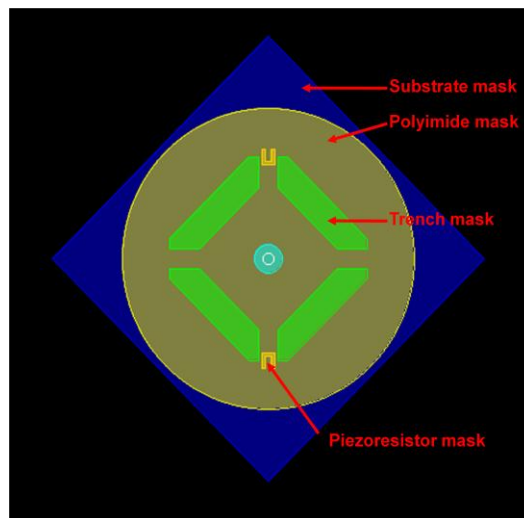


Fig. B.2 Layout of a tactile sensor without superstrate

The process file is crucial as it is first step towards realizing a three-dimensional structure which is shown in Fig. B.3. The three-dimensional structure can be viewed in solid modeler. For the analysis to be done, the structure has to be meshed. For all the simulations that follow, extruded bricks were used. For extrude meshing a 2-D mesh is created by an algorithm which then extrudes the mesh in the z-direction. For this mesh type the algorithm Pave, QMorph and parabolic elemental order are preferred. Paving algorithm is a quadrilateral mesh which generates a 2-D mesh from the boundary of the model towards the center. Parabolic bricks are 27-node bricks (or quadratic interpolation) which give accurate results

when utilized for large structural displacements. For MEMS structures with complex geometries extruded bricks provide accurate results. No shell elements were used. The optimum mesh size obtained after convergence studies is 4 μm . Mesh size for the mesh extrusion in the z-direction of the 3-D model was not used. The meshing size was checked under quality query for optimal average volume mesh size (ranging between 1 to 20). Fig. B.4 shows the meshed solid model of a tactile sensor without superstrate.

Number	Step Name	Layer Name	Material Name	Thickness	Mask Name	Photoresist	Depth
0	Substrate	Substrate	POLYIMIDE	40	SubstrateMask		
1	Stack Material	Passivation	SI3N4	1			
2	Sacrificial	Sacrificial_Poly	POLYIMIDE	6.5			
3	Stack Material	Membrane	AL2O3	1.4			
4	Straight Cut				Patch	-	0.2
5	Planar Fill	Patch	AL2O3	0.1			
6	Straight Cut				Patch	+	0.1
7	Straight Cut				Patch	-	0.1
8	Stack Material	Piezoresistors	NICHROME	0.02			
9	Straight Cut				piezoresistor	+	
10	Straight Cut				poly	-	
11	Straight Cut				Polyimide_5	-	

Fig. B.3 Process-file of a tactile sensor without superstrate

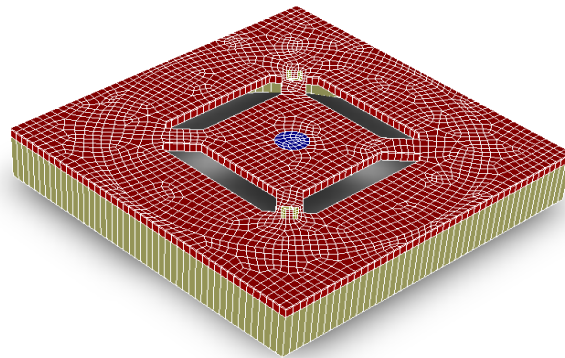


Fig. B.4 Meshed solid model of a tactile sensor without superstrate

Figs. B.5 to Fig. B.7 represent the layout, process and three-dimensional file for the tactile sensor with a superstrate.

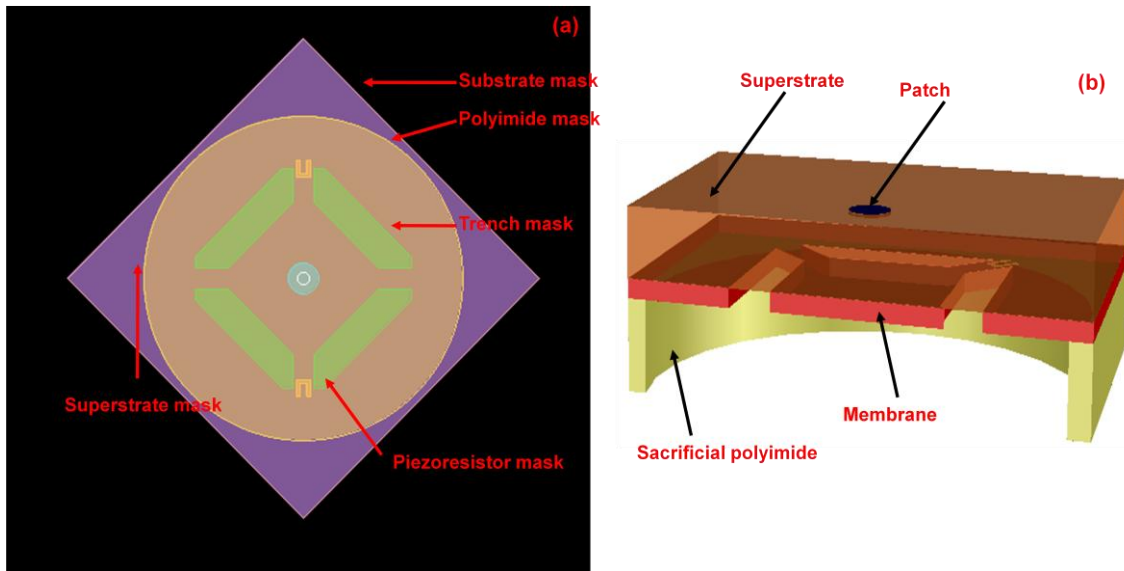


Fig. B.5 (a) Layout of a tactile sensor with superstrate and (b) cut-out of the 3-D model

Number	Step Name	Layer Name	Material Name	Thickness	Mask Name	Photoresist	Depth
0	Substrate	Substrate	POLYIMIDE	40	SubstrateMask		
1	Stack Material	Passivation	SI3N4	1			
2	Sacrificial	Sacrificial_Poly	POLYIMIDE	6.5			
3	Stack Material	Membrane	AL2O3	1.4			
4	Stack Material	Piezoresistors	NICHROME	0.02			
5	Straight Cut				piezoresistor	+	
6	Planar Fill	Superstrate	POLYIMIDE	5			
7	Straight Cut				Patch	-	0.2
8	Planar Fill	Patch	POLYIMIDE	0.1			
9	Straight Cut				Patch	+	0.1
10	Straight Cut				Patch	-	0.1
11	Straight Cut				poly	-	
12	Straight Cut				Polyimide_5	-	

Fig. B.6 Process-file of a tactile sensor with superstrate

The MemMech module is used for simulating the devices. Non-linear analysis is chosen as the membrane undergoes a large deflection in the cavity. For stress analysis studies the additional analysis settings are not required (shown in Fig. B.9). Under MemMech advanced settings the solver memory has been increased to 1500 megabytes. This increase in memory allocation for the solver has greatly helped in attaining simulation results at a quicker pace. Fig.

B.9 to Fig. B.11 show the steps followed in simulating the tactile sensors for with and without a superstrate. The layers in the 3-D model were merged at all times to obtain a continuous mesh. For the surface boundary conditions two different FixTypes were used: fixAll and LoadPatch. When all the degree of freedom of a side surface, edge, node or the face of a model are to be fixed fixAll is selected. LoadPatch is used to specify the value of pressure. LoadValue takes the amount of the load or pressure to be applied on to the structure for mechanical deformation. The units of load are given in MPa.

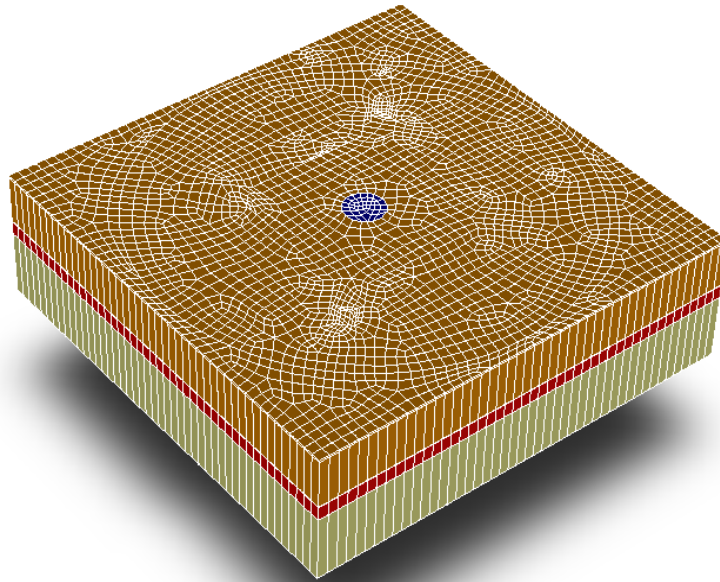


Fig. B.7 Meshed solid model of a tactile sensor with superstrate

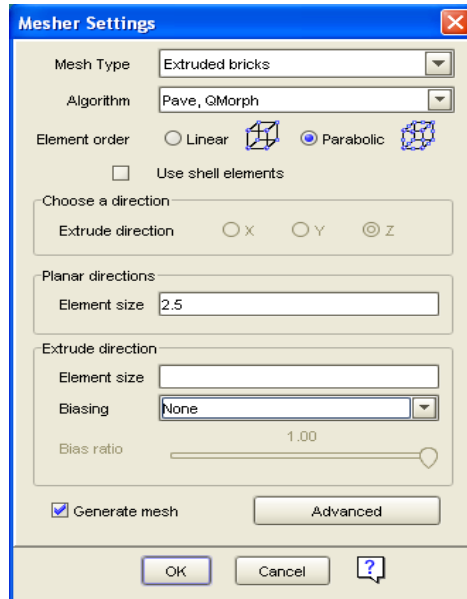


Fig. B.8 Mesher settings

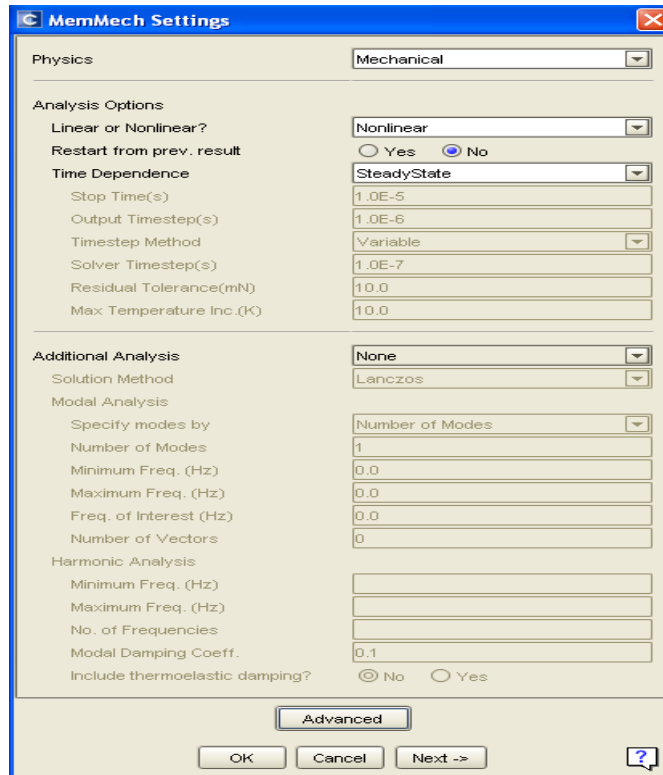


Fig. B.9 MemMech settings

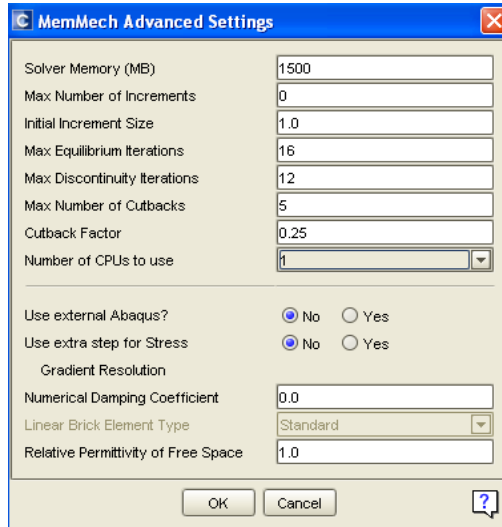


Fig. B.10 MemMech advanced settings

SurfaceBCs	FixType	Patch1	and1	Patch2	and2	Patch3	LoadValue	Variable	Transient	
Set1	fixAll	Fixed	and	none	and	none	Scalar	0.0	Fixed	Fixed
Set2	LoadPatch	Top	and	none	and	none	Scalar	0.1	Fixed	Fixed
Set3	none	none	and	none	and	none	Scalar	0.0	Fixed	Fixed

Fig. B.11 Boundary condition settings

APPENDIX C

FLEXIBLE TACTILE SENSOR CHARACTERIZATION RESULTS

C.1 I-V Characterization Results

I-V characterization was performed by applying a current sweep in the range $\pm 1 \times 10^{-4}$ A. The individual resistances presented in Tables 4.1 and 4.2 for the tactile sensors without and with a superstrate are plotted in Figs. C.1 to C.8.

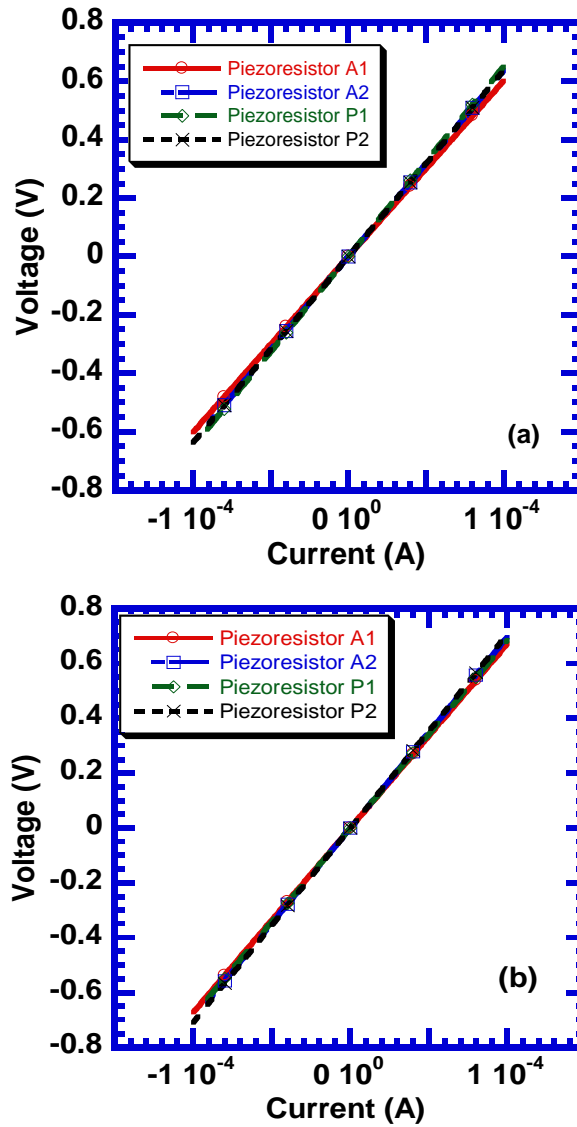


Fig. C.1 Voltage and current characteristics for T1 without superstrate (a) Device # I and (b) Device # II

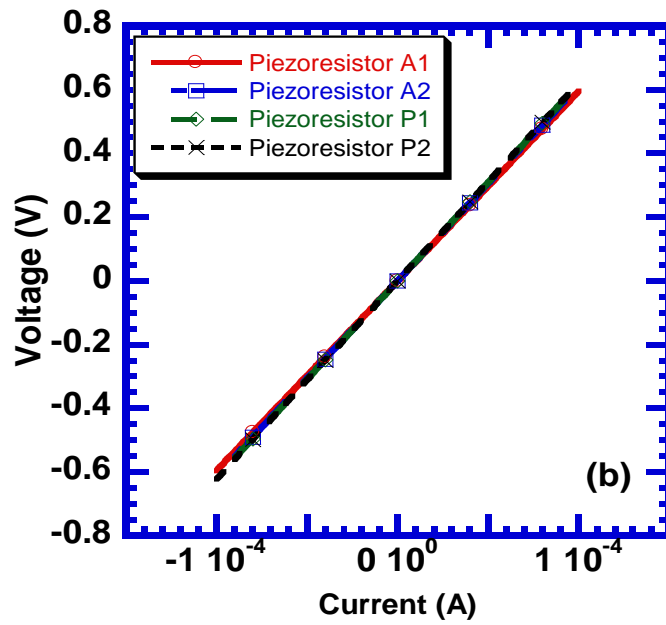
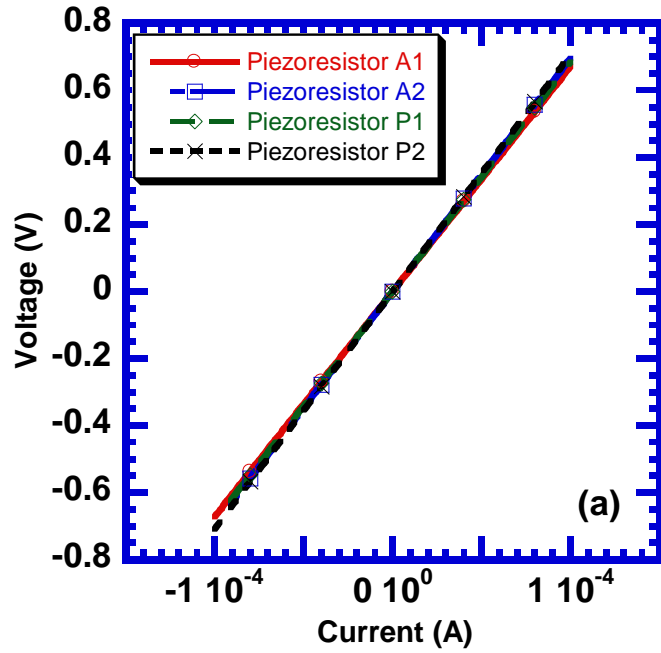


Fig. C.2 Voltage and current characteristics for T2 without superstrate (a) Device # I and (b) Device # II

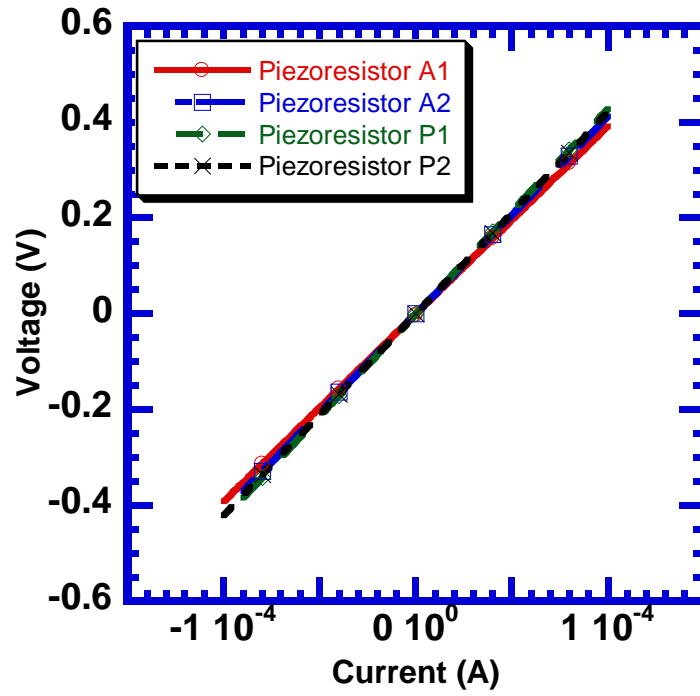


Fig. C.3 Voltage and current characteristics for T3 without superstrate Device # 1

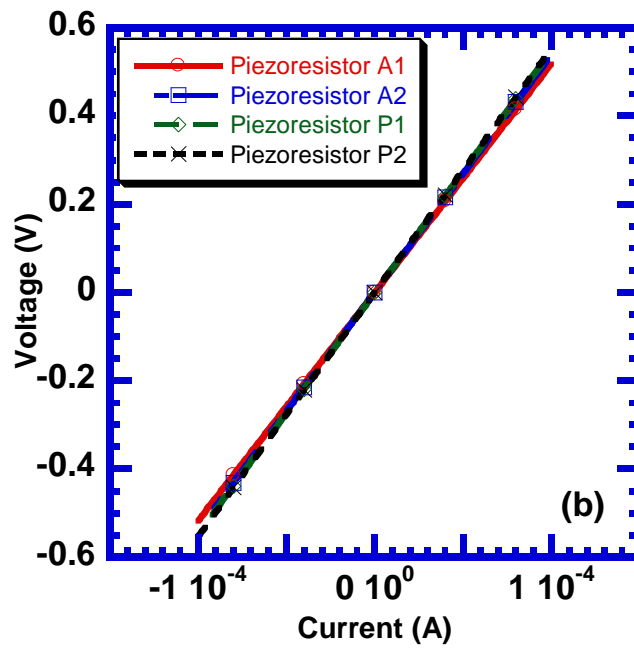
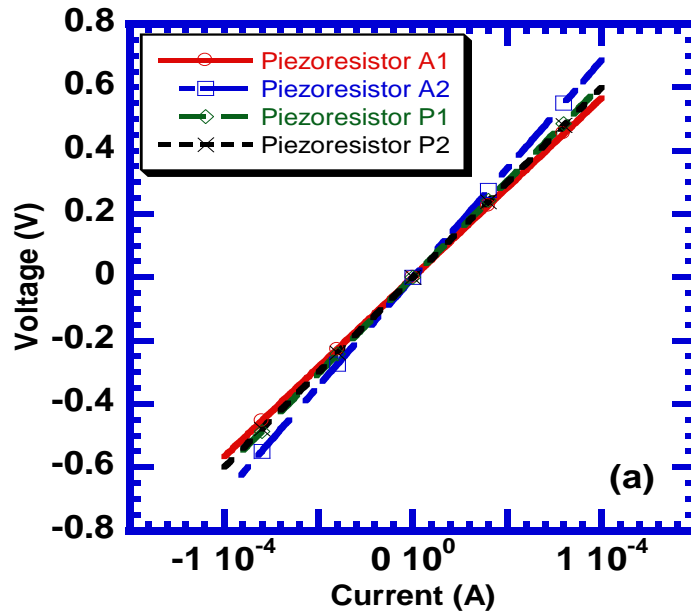


Fig. C.4 Voltage and current characteristics for T4 without superstrate (a) Device # I and (b) Device # II

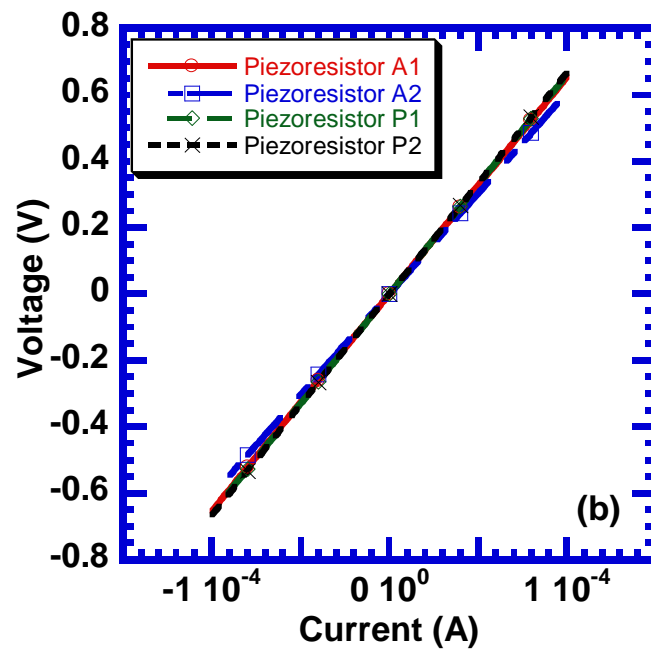
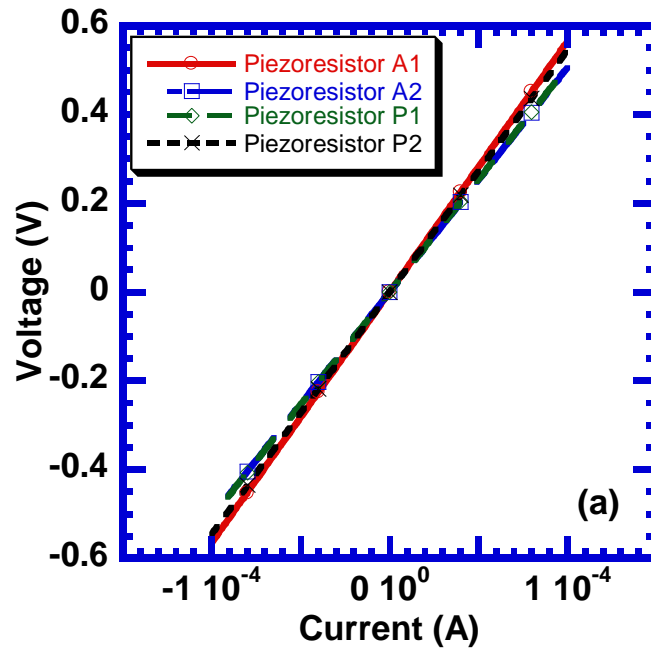


Fig. C.5 Voltage and current characteristics for T1 with superstrate (a) Device # I and (b) Device # II

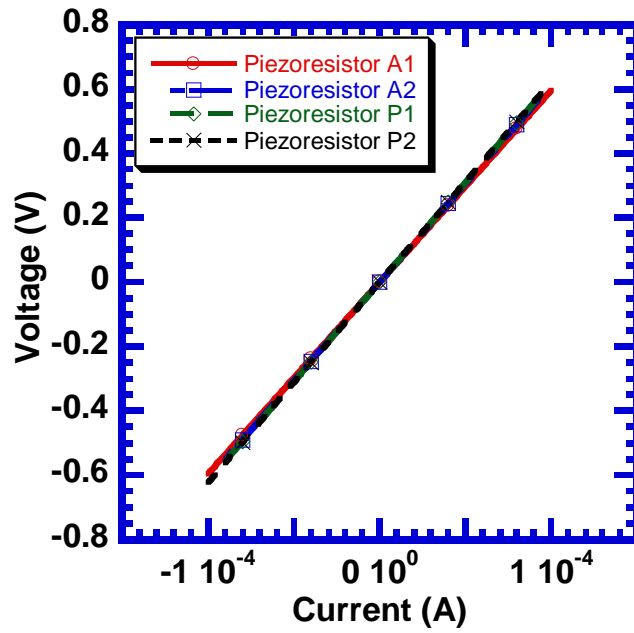


Fig. C.6 Voltage and current characteristics for T2 with superstrate Device # 1

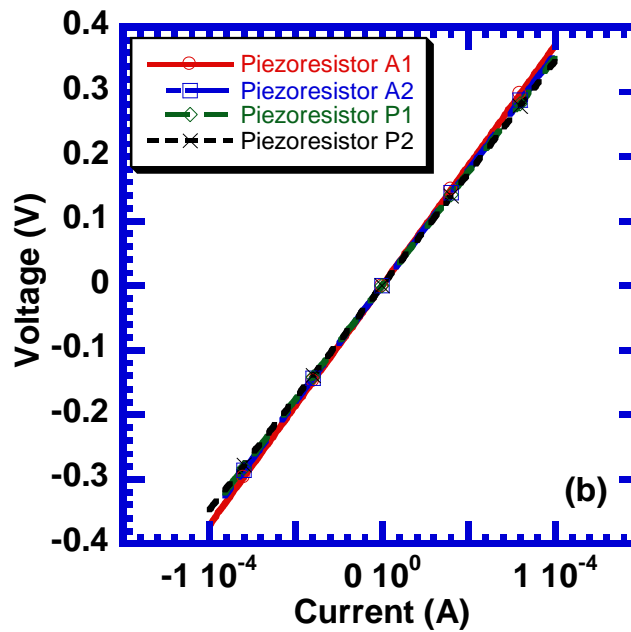
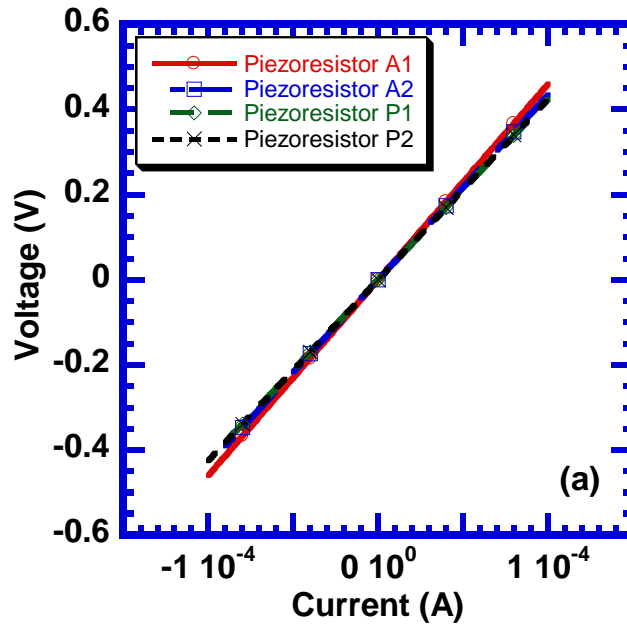


Fig. C.7 Voltage and current characteristics for T3 with superstrate (a) Device # I and (b) Device # II

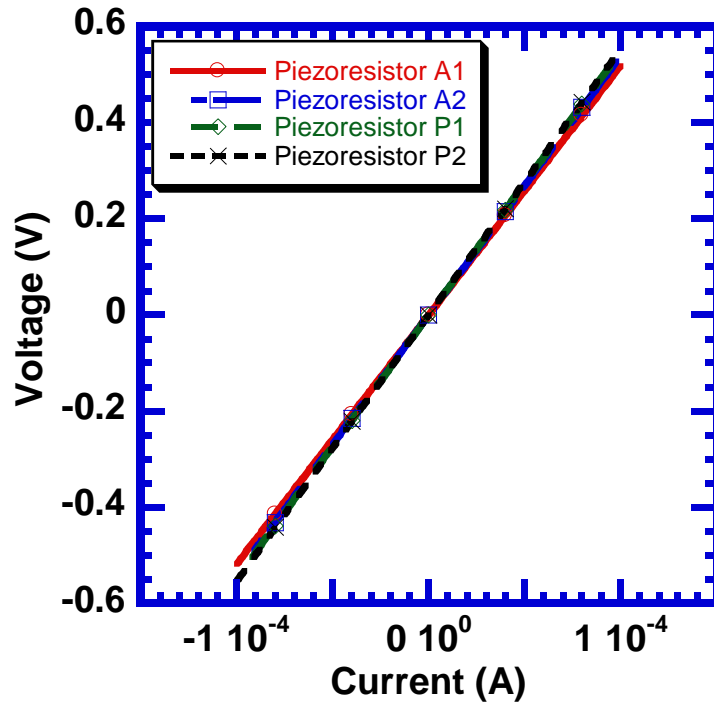


Fig. C.8 Voltage and current characteristics for T4 with superstrate Device # 1

REFERENCES

- [1] T. Loher, R. Vieroth, M. Seckel, A. Ostmann, and H. Reichl, "Stretchable electronic systems for wearable and textile applications," *Proc. IEEE 9th VLSI Packaging Workshop in Japan*, pp. 9-12, 2008.
- [2] H. K. Lee, S. I. Chang, and E. Yoon, "A flexible polymer tactile sensor: Fabrication and modular expandability for large area deployment," *J. Microelectromech. Sys.*, vol. 15, no. 6, pp. 1681-1686, 2006.
- [3] T. V. Papakostas, J. Lima, and M. Lowe, "A Large Area Force Sensor for Smart Skin Applications," *Proc. IEEE Sensors*, vol. 2, pp.1620-1624, 2002.
- [4] C. Liu, *Foundations of MEMS*, Pearson Prentice Hall, ISBN 0-13-147286-0, 2006.
- [5] S. Najarian, J. Dargahi, and A. A. Mehrizi, *Artificial tactile sensing in biomedical engineering*, McGraw-Hill, ISBN 978-0-07-160151-1, 2009.
- [6] M. H. Lee, "Tactile sensing: New directions, New Challenges," *International Journal of Robotics Research*, vol. 19, no. 7, pp. 636-643, 2000.
- [7] M. R. Wolfenbuttel, and P. P. L. Regtien, "Polysilicon bridges for the realization of tactile sensors," *Sensors and Actuators A-Phys.*, vol. 26, pp. 257-264, 1991.
- [8] D. J. Beebe, A. S. Hsieh, D. D. Denton, R. G. Radwin, "A silicon force sensor for robotics and medicine," *Sensors and Actuators A-Phys.*, vol. 50, pp. 55-65, 1995.
- [9] B. J. Kane, M. R. Cutkosky, and G. T. A. Kovacs, "A Traction Stress Sensor Array for Use in High-Resolution Robotic Tactile Imaging," *J. Microelectromech. Sys.*, vol. 9, no. 4, pp. 425-434, 2000.
- [10] J. Engel, J. Chen, and C. Liu, "Development of polyimide flexible tactile sensor skin," *J. Micromech. Microeng.*, vol. 13, pp. 359-366, 2003.

- [11] K. Takei, T. Takahashi, J. C. Ho, H. Ko, A. G. Gillies, P. W. Leu, R. S. Fearing, and A. Javey, "Nanowire active matrix circuitry for low-voltage macroscale artificial skin," *Nature Materials*, vol. 9, pp. 821-826, 2010.
- [12] S. K. Patil, Z. Çelik-Butler, and D. P. Butler, "Nanocrystalline Piezoresistive Polysilicon Film by Aluminium-Induced crystallization for Pressure-Sensing Applications," *IEEE Transactions on Nanotechnology*, vol. 9, no. 5, 2010.
- [13] L. Lin and W. Yun, "MEMS pressure sensors for aerospace applications," in *Proc. IEEE Aerospace Conf.*, Mar. 1998, pp. 429-436.
- [14] C. Malhaire and D. Barbier, "Design of a polysilicon-on-insulator pressure sensor with original polysilicon layout for harsh environment," *Thin Solid Films.*, vol. 427, pp. 362–366, Mar. 2003.
- [15] H. C. Lim, B. Schulkin, M. J. Pulickal, S. Liu, R. Petrova, G. Thomas, S. Wagner, K. Sidhu, and J. F. Federici, "Flexible membrane pressure sensor," *Sens. Actuators A*, vol. 119, pp. 332–335, Apr. 2005.
- [16] Y. Zhang, B. Liu, L. Liu, Z. Tan, Z. Zhang, H. Lin, and T. Ren, "Design, fabrication and characterization of novel piezoresistive pressure microsensor for TPMS," in *Proc. IEEE Asian Solid State Circuits Conf.*, Nov. 2006, pp. 443–446.
- [17] S. Chen, M.-Q. Zhu, B.-H. Ma, and W.-Z. Yuan, "Design and optimization of micro piezoresistive pressure sensor," in *Proc. 3rd IEEE Intl. Conf. Nano/Micro Engineered Mol. Sys.*, Jan. 2008, pp. 351–356.
- [18] K. Saejok, B. P. E. Chaowicharat, E. Ratanaudomphisut, O. Treethaveesak, C. Hruanun, and A. Poyai, "Effect of temperature to characteristics of polysilicon based surface micromachining piezoresistive pressure sensor," in *Proc. 5th IEEE Intl. Conf. ECTI-CON*, May 2008, vol. 2, pp. 813–816.
- [19] X. Liu, X. Lu, R. Chuai, C. Shi, and C. Suo, "Polysilicon nanofilm pressure sensor," *Sens.*

Actuators A, vol. 154, pp. 42–45, Aug. 2009.

[20] K. Gilleo, *Handbook of Flexible Circuits*, Van Nostrand Reinhold, ISBN 0-442-00168-1, 1991.

[21] W. S. Wong and A. Salleo, *Flexible electronics: Materials and applications*, Springer Science and Business Media, ISBN 978-0-387-74362-2, 2009.

[22] S. Wagner, H. Gleskova, I-C. Cheng, J. C. Sturm, and Z. Sou, “Mechanics of TFT technology on flexible substrates,” *Flexible Flat Panel Displays*, edited by G. P. Crawford, Wiley Imprint, ISBN 0-470-87048-6, 2005.

[23] S. Beeby, G. Ensell, M. Kraft, N. White, *MEMS Mechanical Sensors*, Artech House, ISBN 1-58053-536-4, 2004.

[24] R. Hagen, “Choosing the Right Low-Pressure Sensor,” *Sensors*, <http://www.sensormag.com>, 1998.

[25] C. S. Smith, “Piezoresistance effect in germanium and silicon,” *Phys. Rev.*, vol. 94, no. 1, pp. 42-49, 1954.

[26] E. N. Adams, “Elastoresistance in p-type Ge and Si”, *Phys. Rev.*, vol. 96, no. 3, pp. 803-804, 1954.

[27] C. J. Reilly, and J. E. Sanchez, “The piezoresistance of aluminum alloy interconnect structures,” *J. Appl. Phys.*, vol. 85, no. 3, pp. 1943-1948, 1999.

[28] C. Hu, Y. Gao, and Z. Sheng, “The piezoresistance coefficients of copper and copper-nickel alloys,” *J. Mat. Sci.*, vol. 35, no. 2, pp. 381-386, 2000.

[29] A. A. Barlian, W. T. Park, J. R. Mallon, A. J. Rastegar, and B. L. Pruitt, “Review: Semiconductor piezoresistance for Microsystems,” *Proc. IEEE*, vol. 97, no. 3, pp. 513-552, 2009.

[30] A. L. Window, and G. S. Holister, *Strain gauge technology*, Applied Science Publishers, ISBN 0-85334-118-4, 1982.

- [31] P. J. French, and A. G. R. Evans, "Polycrystalline silicon as a strain gauge material," *J. Phys. E: Sci. Instrum.*, vol. 19, pp. 1055-1058, 1986.
- [32] S. D. Senturia, *Microsystem Design*, Kluwer Academic Publishers, ISBN 0-7923-7246-8, 2002.
- [33] S. M. Sze, *Semiconductor Sensors*, Wiley-Interscience Publication, ISBN 0-471-54609-7, 1994.
- [34] M. A. Angadi, and R. Whiting, "Longitudinal and transverse strain sensitivity of nichrome films," *Mater.Sci. Eng.:B*, vol. 7, pp. L1–L4, 1990.
- [35] J. Engel, J. Chen, and C. Liu, "Polymer-Based MEMS Multi-Modal Sensory Array," *226th National Meeting of the American Chemical Society*, vol. 44(2), pp. 534-535, 2003.
- [36] J. Yan, and J. Zhou, "Strain sensitivity and temperature influence of Nichrome (80/20 wt.%) thin film fabricated by magnetron sputtering," *International Journal of Modern Physics B*, vol. 21, no. 21, pp. 3719-3731, 2006.
- [37] I. H. Kazi, P. M. Wild, T. N. Moore, and M. Sayer, "The electromechanical behavior of nichrome (80/20 wt.%) film," *Thin Solid Films*, vol. 433, pp.337–343, 2003.
- [38] A. Garcia-Alonso, J. Garcia, E. Castano, I. Obieta, and F. J. Gracia, "Strain sensitivity and temperature influence on sputtered thin films for piezoresistive sensors," *Sensors and Actuators A: Phy.*, vol. 37-38, pp. 784-789, 1993.
- [39] R. Ramesham, and R. Ghaffarian, "Challenges in interconnection and packaging of Microelectromechanical Systems (MEMS)," *Proc. 50th Electronic Components and Technology Conference*, pp. 666-675, 2000.
- [40] R. R. Tummala, *Fundamentals of Microsystems Packaging*, Mc-Graw Hill, ISBN 0-07-141807-5, 2000.
- [41] G. Blasquez, P. Pons, and A. Boukabache, "Capabilities and limits of silicon pressure sensors," *Sensors and Actuators*, vol. 17, pp. 287-403, 1989.

- [42] T. R. Hsu, *MEMS and Microsystems*, Wiley-Interscience Publication, ISBN 978-0-470-08301-7, 2008.
- [43] I. E. Gonenli, "Failure Assessment in Aerospace Systems via Integrated Multi-functional Sensors," University of Texas at Arlington, 2010.
- [44] J. F. Shackelford, W. Alexander, *CRC Materials Science and Engineering Handbook*, CRC Press, 2001.
- [45] D. T. Read, Y. W. Cheng, R. R. Keller, and J. D. McColskey, "Tensile properties of free-standing aluminum thin films," *Scripta Materialia*, vol. 45, pp. 583-589, 2001.
- [46] J. Tamayo, A. Humphris, A. Malloy, and M. Miles, "Chemical sensors and biosensors in liquid environment based on microcantilevers with amplified quality factor," *Ultramicroscopy*, vol. 86, pp. 167-173, 2001.
- [47] J. Li, M. Kahrizi, and L. Landsberger, "Design, fabrication and characterization of CMOS-compatible optical microswitches," *IEEE Conf. Proc.*, vol. 1, pp. 319–22, 2003.
- [48] K. E. Petersen, "Silicon as a Mechanical Material," *Proceedings of IEEE*, vol. 70, no.5, pp.421, 1982.
- [49] Z. Xue, Y. Huang, and M. Li, "Particle size effect in metallic materials: a study by the theory of mechanism-based strain gradient plasticity," *Acta Materialia*, vol. 50, pp. 149-160, 2002.
- [50] H. A. Mansy, J. R. Grahe and R. H. Sandler, "Elastic Properties of synthetic materials for soft tissue modeling," *Phys. Med. Biol.*, vol. 53, pp. 2115-2130, 2008.
- [51] J. F. Shackelford, W. Alexander, *Materials Science and Engineering Handbook*, CRC Press LLC, ISBN 0-8493-2696-6, 2001.
- [52] G. P. O'Hara, "Mechanical properties of silicone rubber in a closed volume," Large Caliber Weapon Syst. Lab., Army Armament Res. Dev. Cent., Watervliet, NY, USA. Avail. NTIS. Report (1983), (ARLCB-TR-83045, SBI-AD-E440224; Order No. AD-A138129), pp. 21 From: Gov. Rep. Announce. Index (U. S.) 1984, 84(11), 129.

[53] T. Thome, S. Fouchez, S. Delalande, "Determination of silicone coating Young's modulus using atomic force microscopy," *Physica B*, Vol. 404, pp. 22–25, 2009.

BIOGRAPHICAL INFORMATION

Rohit Kilaru received his B.Tech in electronics and communications engineering from S.R.M. University, Chennai, India, in 2007. He is currently working towards his M.S. degree in electrical engineering from the University of Texas (UTA), Arlington, TX. Since summer 2008, he has been pursuing his research goals working at the Microsensors Lab and at The Nanotechnology Research and Teaching Facility at UTA. His research interests include simulation and fabrication of actuators and sensors, fuel cells and characterization techniques.